Available online at www.sciencedirect.com

ScienceDirect

Journal of Magnesium and Alloys xxx (xxxx) xxx

www.elsevier.com/locate/jma

Full Length Article

The effect of grain size and rolling reduction on microstructure evolution and annealing hardening response of a Mg-3Gd alloy

F. Han[a], X. Luo[a,b], Q. Liu[a], Z. Hou[a,*], K. Marthinsen[c], G.L. Wu[d], C. Hatzoglou[c], P. Kontis[c], X. Huang[a,e,*]

[a] *International Joint Laboratory for Light Alloys (MOE), College of Materials Science and Engineering, Chongqing University, Chongqing 400044, China*
[b] *Key Laboratory for Light-Weight Materials, Nanjing Tech University, Nanjing 210009, China*
[c] *Department of Materials Science and Engineering, Norwegian University of Science and Technology, Trondheim 7491, Norway*
[d] *Beijing Advanced Innovation Center for Materials Genome Engineering, University of Science and Technology Beijing, Beijing 100083, China*
[e] *Shenyang National Laboratory for Materials Science, Chongqing University, Chongqing 400044, China*

Received 1 June 2023; received in revised form 8 September 2023; accepted 15 September 2023
Available online xxx

Abstract

Mg-3Gd (wt.%) samples with different initial grain sizes were prepared to evaluate the grain size effect on microstructural evolution during cold rolling and subsequent annealing hardening response. The deformation behavior and mechanical response of the as-rolled and annealed samples were systematically investigated by a combination of electron microscopy and microhardness characterization. The results show that the twinning activities were highly suppressed in the fine-grained samples during rolling. Upon increasing the rolling reduction to 40%, ultra-fine grain structures with a volume fraction of ~28% were formed due to the activation of multiple slip systems. Conversely, twinning dominated the early stages of deformation in the coarse-grained samples. After a 10% rolling reduction, numerous twins with a volume fraction of ~23% were formed. Further increasing the rolling reduction to 40%, high-density dislocations were activated and twin structures with a volume fraction of ~36% were formed. The annealing hardening response of deformed samples was effectively enhanced compared to that of the non-deformed samples, which was attributed to the enhanced Gd segregation along grain boundaries, twin boundaries and dislocation cores. Moreover, the grain size and rolling reduction were found to affect the microstructure evolution during annealing, resulting in a notable difference in the annealing hardening response of Mg-3Gd alloy between samples of different grain sizes deformed to different strains. These findings highlight the crucial importance of microstructural and processing parameters in the design of high-strength, cost-effective Mg alloys.

Keywords: Mg-Gd alloy; Grain size effect; Deformation mechanism; Microstructural evolution; Annealing hardening.

1. Introduction

With the urgency of energy conservation and pollution emission reduction in recent years, magnesium (Mg) alloys have attracted extensive attention due to their high specific strength [1–3]. However, hexagonal close-packed (HCP) crystal-structured Mg alloys offer an insufficient number of slip systems and inherent high deformation anisotropy [4,5], resulting in poor formability and low strength at room temperature, which limits their widespread applications [6]. Therefore, high-strength Mg alloys have been extensively studied through structural refinement [7,8]. It is generally considered that Mg alloys exhibit intrinsic weak and slow age hardening response [9,10]. However, it is notable that the ultimate solubility of rare earth (RE) elements in the Mg matrix is very high and decreases exponentially with decreasing temperature. This may indicate a potentially excellent age hardening response for rare earth-containing Mg alloys [11–13]. There-

* Corresponding authors.
E-mail addresses: houzy@cqu.edu.cn (Z. Hou), xiaoxuhuang@cqu.edu.cn (X. Huang).

https://doi.org/10.1016/j.jma.2023.09.025

fore, RE elements, such as Gd, Y, Nd and Dy, have been added to Mg alloys for precipitation strengthening. Previous results have shown that either an abundance of RE elements addition and/or a long aging time is required to form the dispersion of precipitates [11]. The most encouraging discovery is that deformation before annealing can effectively accelerate and enhance the hardening response due to significant solute segregation along various boundaries, such as grain boundaries (GBs), twin boundaries (TBs) and dislocation boundaries, during processing and subsequent annealing [14–16].

For HCP Mg alloys, the effect of initial grain size and processing methods (deformation mode and processing parameters) on the deformation mechanisms/microstructures should be taken into consideration during plastic deformation [17–21]. Simulation results and experimental observations in polycrystalline Mg alloys have shown that the activation of different deformation mechanisms strongly relies on the grain size [22,23]. Luo et al. [24] have reported that, in the Mg-3Gd (wt.%) alloy, ⟨a⟩ and ⟨c + a⟩ dislocations dominate the microstructure in the fine-grained samples with grain size smaller than 5 μm, while ⟨a⟩ dislocations and {$10\bar{1}2$} tension twins dominate the microstructure in the coarse-grained samples with grain size larger than 10 μm at the early stage of deformation [24]. The changes in the deformation mechanisms due to the grain size effect inevitably lead to differences in microstructural characteristics of deformed Mg alloys. The microstructural evolution of Mg alloys may also be affected by processing parameters [19,20,25]. Based on the aforementioned grain size effect, all twinning systems are hindered and basal and non-basal slip modes can be activated to satisfy the von Mises criterion in the fine-grained Mg alloys [24,26]. However, the basal ⟨a⟩ slip and {$10\bar{1}2$} tension twinning are easily activated and dominate the microstructure evolution in the coarse-grained Mg alloys after being subjected to a small deformation [27–29]. Multiple dislocation slips and various twinning systems are activated with increasing deformation degree. Hence, high-strain plastic deformation promotes the formation of dislocation cells, twin structures, and even nano-grains [30,31]. The structural refinement mechanisms and the volume fractions of these structural features mainly depend on the deformation magnitude and dominant deformation mechanisms in Mg alloys. That is, both initial grain size and deformation degree may lead to a significant difference in the deformation microstructures of Mg alloys, likely affecting the solute segregation and subsequent annealing hardening response.

Compared with the precipitation hardening in Mg alloys, the hardening response caused by solute segregation along boundaries is rapid and yet weak [16,32]. However, a deformation step before annealing would enhance the hardening kinetics by promoting solute segregation and cluster formation, resulting in significant enhancement of microhardness and strength of Mg alloys after annealing [16,33,34], especially in Mg-RE alloys. The phenomenon mentioned above, i.e., deformed Mg alloys mainly strengthened by solute segregation and clusters during annealing, has been defined as "annealing hardening/strengthening response" [14,16,34-36]. The enhanced annealing hardening response is mainly caused by solute segregation at internal defects such as a high density of dislocation boundaries, GBs, TBs and stacking faults (SFs) [33,37,38]. After deformation, therefore, combined with subsequent annealing, the matrix of Mg alloys can easily facilitate and enhance the segregation of solute atoms, the formation of a large number of clusters and GP zones, leading to a rapid increase of microhardness and strength [12,35,39]. We previously found an apparent hardening response and clear evidence of Gd segregation towards dislocations, GBs and TBs in the annealed sample compared with the hot-rolled Mg-3Gd (wt.%) alloy [14], demonstrating that deformation combined with annealing is a feasible approach to strengthen/harden dilute Mg-Gd alloys.

Nevertheless, it remains to be established how the initial grain size influences the microstructural evolution and the annealing hardening response of Mg alloys with various degrees of pre-deformation. Hence, in the present work, fully recrystallized fine-grained (FG) and coarse-grained (CG) samples of an Mg-3Gd alloy were prepared by large strain hot rolling (LSHR) and different annealing treatments. The effect of initial grain size and rolling reduction on the microstructural evolution and their subsequent annealing hardening response were thoroughly elucidated and discussed.

2. Experimental

2.1. Sample preparation and annealing process

A Φ82 mm Mg-3Gd (wt.%) alloy ingot was held at 450 °C for 24 h for homogenization treatment. After preheating at 450 °C for 2 h, the ingot was extruded into a 5 mm-thickness plate (see Fig. 1). The plate with dimensions of 75 × 30 × 5 mm^3 was then subjected to large strain hot rolling (LSHR) with two passes after annealing at 500 °C for 3 h. It was preheated at 400 °C for 10 min before each rolling pass, and the total rolling reduction was 70%. The LSHR-processed sheets were finally annealed at 320 °C for 1 h or at 450 °C for 3 h to obtain initial samples with two different recrystallized average grain sizes, 3.5 μm (FG sample) and 54 μm (CG sample), (see Fig. 2). All samples were water quenched after hot rolling and annealing. The textures of the FG and CG samples (Figs. 2b and 2e) are similar with their basal poles tilting from the normal reduction (ND) towards the rolling direction (RD). Both the FG and CG samples were further cold rolled to five different rolling reductions, 5%, 10%, 20%, 40% and 60%, at room temperature (denoted as FGcr5%, FGcr10%, FGcr20%, FGcr40%, FGcr60%, CGcr5%, CGcr10%, CGcr20%, CG40% and CGcr60%, correspondingly). The rolling reduction per pass was within 5 − 8% to avoid any serious edge cracking. The initial sample (without cold rolling) and the samples cold rolled to 0 − 60% were isochronally annealed for 1 h in a temperature range from 100 °C to 500 °C. Moreover, the initial and the samples cold rolled to 10% and 40% were isothermally annealed at 150, 200 and 250 °C, for 20 min to 100 h (see Fig. 1).

Please cite this article as: F. Han, X. Luo, Q. Liu et al., The effect of grain size and rolling reduction on microstructure evolution and annealing hardening response of a Mg-3Gd alloy, Journal of Magnesium and Alloys, https://doi.org/10.1016/j.jma.2023.09.025

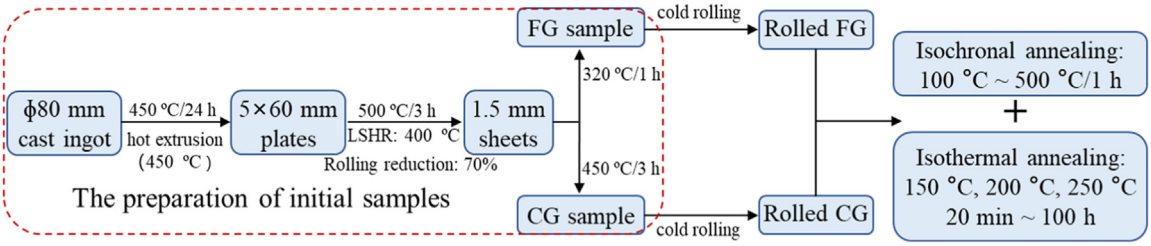

Fig. 1. Schematic of process and annealing treatment of Mg-3Gd samples. LSHR: large strain hot rolling; FG: fine-grained; CG: coarse-grained.

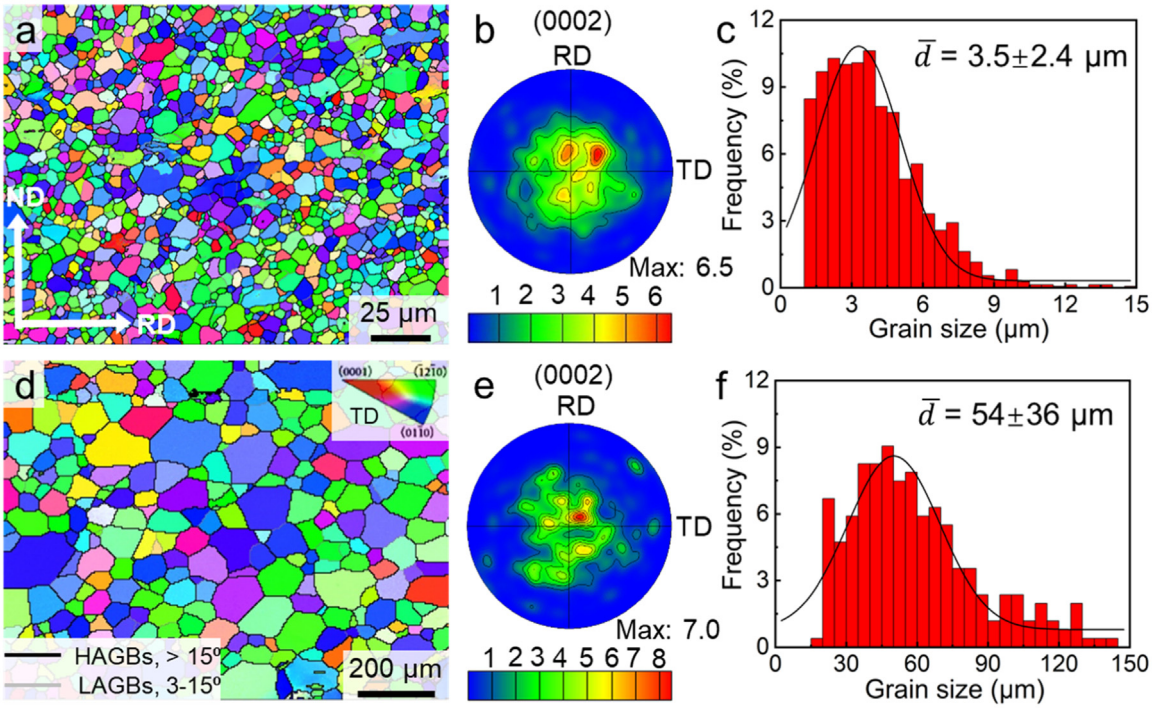

Fig. 2. EBSD inverse pole figure (IPF) maps (a, d), corresponding (0002) pole figures (b, e) and grain size distributions (c, d) fitted by the Gaussian function of FG sample ($a - c$) and CG sample ($d - f$). The high angle grain boundaries (HAGBs) with misorientation angles above 15° and low angle grain boundaries (LAGBs) with misorientation angles between 3° and 15° are colored by black and gray lines, respectively. Observation along TD is applied to IPF triangle.

2.2. Vickers microhardness tests and microstructural characterization

The microhardness of each sample was averaged from 15 indentations measured using a Vickers microhardness tester (HMV-G21ST) with a static load of 490 mN (50 g) and a dwell time of 10 s. To directly compare the contribution of annealing hardening between different cases, the relative microhardness increment (ΔHV), defined as $HV_{\text{after}} - HV_{\text{before}}$, was evaluated. HV_{before} and HV_{after} are the microhardness before and after annealing, respectively.

The microstructure characterization was performed using a scanning electron microscope (SEM, JEOL JSM-7800F) operated at 20 kV, equipped with an electron backscatter diffraction (EBSD) detector. Before the EBSD characterization, samples were ground mechanically and then polished electrochemically in an electrolyte of 10 vol.% perchloric acid ($HClO_4$) and 90 vol.% ethanol (C_2H_5OH) with a constant voltage of 20 V at –30 °C. The microhardness and microstructure were examined on the RD-ND plane of the sample. The EBSD data were analyzed using HKL Channel 5 software.

A transmission electron microscope (TEM, JEOL JEM-2100) operated at 200 kV and a spherical aberration-corrected scanning transmission electron microscope (STEM, FEI Titan G2 60–300) in high angle annual dark field (HAADF)-STEM mode operated at 300 kV were used to investigate the microstructural evolution in detail. The cross-sectional thin foils for TEM observations were prepared by mechanically grinding to a thickness of 50 μm and punching into 3 mm-wide discs, subsequently using Ar precision ion polishing (Gatan PIPS 695) at –70 °C. The average grain size of ultra-fined grains (UFGs) in the TEM microstructures was obtained from the equivalent circle diameter, and the twin thickness of twin structures was measured perpendicular to the twin boundaries using Image-Pro-Plus 6.0 software. The total surface area per volume of boundaries (S_{total}) and the equivalent grain size (D_{E}) were calculated based on the EBSD and TEM results. For the equiaxed grain structure, the S_{total} of non-deformed

Please cite this article as: F. Han, X. Luo, Q. Liu et al., The effect of grain size and rolling reduction on microstructure evolution and annealing hardening response of a Mg-3Gd alloy, Journal of Magnesium and Alloys, https://doi.org/10.1016/j.jma.2023.09.025

FG and CG samples can be expressed as [40,41]:

$$S_{\text{total}} = S_{\text{GB}} = 2/D_{\text{R}} \tag{1}$$

where D_{R} is the average grain size of the recrystallized grains. Therefore, the D_{E} can be calculated by the relationship:

$$D_{\text{E}} = \frac{2}{S_{\text{total}}} \tag{2}$$

For the deformed samples, the surface areas of the UFG structures (S_{UFG}) and twin structures (S_{twin}) can be expressed as follows:

$$S_{\text{UFG}} = \frac{\pi}{2D_{\text{UFG}}} Vol.^{\text{UFG}} \tag{3}$$

$$S_{\text{twin}} = \frac{1}{D_{\text{twin}}} Vol.^{\text{twin}} \tag{4}$$

And the surface area of residual GBs (S_{GB}) due to deformation is:

$$S_{\text{GB}} = \frac{2}{D_{\text{R}}}\left(1 - Vol.^{\text{UFG}} - Vol.^{\text{twin}}\right) \tag{5}$$

Therefore, the total surface area per volume of boundaries can be calculated as follows:

$$S_{\text{total}} = S_{\text{GB}} + S_{\text{UFG}} + S_{\text{twin}} \tag{6}$$

To evaluate the segregation of solutes at grain boundaries, specimens for atom probe tomography (APT) were prepared by following a site specific lift-out protocol described in Ref. [42]. An FEI dual beam Helios G4 UX was used for the APT sample preparation. The APT specimens were analyzed using a Cameca LEAP 5000 XS instrument operating at 60 pJ laser energy, 250 kHz and 40 K. The commercial package IVAS 3.8.10 was used for data reconstruction and analysis.

X-ray diffraction (XRD, a Rigaku D/MAX-2500 PC) was performed using Cu-Kα radiation to analyze the difference in dislocation density between rolled and annealed samples. With the help of the Material Analysis Using Diffraction (MAUD) software using XRD line broadening analysis [43,44], the crystallite size (D_{c}) and micro-strain ($<\varepsilon^2>^{1/2}$) were measured. Then, the dislocation density ρ was calculated by:

$$\rho = \frac{2\sqrt{3} < \varepsilon^2 >^{1/2}}{D_{\text{c}} b} \tag{7}$$

where b is the length of Burgers vector for the HCP Mg alloys, i.e. 0.3197 nm [44]. In addition, the lattice axial ratio (c/a) was also estimated using MAUD software. More detailed information on this XRD analysis was previously described in Refs. [45,46].

3. Results

3.1. Microstructures of deformed samples

3.1.1. EBSD microstructures

Fig. 3 shows KAM (Kernel Average Misorientation) maps coupled with various TBs of the rolled FG and CG samples. The non-indexed black regions are associated with high localized stress concentration of rolled samples, and a more detailed analysis of deformation microstructures in the rolled samples will be given in Section 3.1.2. Three types of deformation twins, i.e., $\{10\bar{1}2\}$ 86°±5° $<11\bar{2}0>$ tension twins (TTWs), $\{10\bar{1}1\}$ 56°±5° $<11\bar{2}0>$ compression twins (CTWs) and $\{10\bar{1}2\}-\{10\bar{1}1\}$ 38°±5° $<11\bar{2}0>$ double twins (DTWs), are identified and represented by red, green and fuchsia lines, respectively. Obviously, the initial grain size and rolling reduction strongly affect the microstructural characteristics of the rolled FG and CG samples. Microstructural refinement becomes more remarkable in the FG and CG samples with increasing rolling reduction. More non-indexed black regions and narrow band-like structures appear, especially in the rolled FG samples. Moreover, in both rolled samples, twins of various kinds have formed in the deformed grains. However, the twins in the rolled FG samples are much fewer and shorter than those in the rolled CG samples, as shown in Figs. 3*a*−*d*. Besides, CTW-ing and DTW-ing are highly inhibited in the rolled FG samples, although the rolling reduction is the same for the FG and CG samples. Even after 40% rolling reduction, the FG sample only develops a very low volume fraction of CTWs and DTWs. While a much larger amount of deformation twins is observed in the deformed grains of the rolled CG samples, which initiate from GBs on the one side and terminate inside grains or at GBs on the other side. In the low strain (5% and 10% rolling reductions) samples, most of the twins are TTWs due to the lowest critical resolved shear stress (CRSS) among all deformation twins, while a few CTWs and DTWs are also observed, which leads to a significant grain refinement, as shown in Figs. 3e and 3f). As rolling reduction increases to 20% and 40%, the length of TTW boundaries decreases rapidly and plenty of DTWs appear, as shown in Figs. 3g and h. Therefore, a remarkable grain size effect on the twinning behavior of Mg alloys is seen, consistent with previous reports [26,47].

3.1.2. TEM microstructures

Fig. 4 shows representative TEM images of FGcr10% and CGcr10% samples. Two different characteristic features are observed in the deformation microstructure of FGcr10% and CGcr10% samples, which are classified as dislocation structures and twin structures. As shown in Fig. 4a, typical dislocation structures with a lot of dislocation entanglements are present within the deformed fine grains in the FGcr10% sample, while twinning behavior is strongly inhibited. Only a few deformation twins are observed. Based on the quantitative structural parameters of rolled FG and CG samples in Table 1, it can be seen that the volume fraction of twin structures in the FGcr10% sample is only 5% and the average twin thickness is 212 ± 140 nm. Most regions of the FGcr10% sample are dislocation structures, as shown in Figs. 4a and 4b. Fig. 4c shows a weak-beam dark-field image of dislocations magnified from the red dashed frame of Fig. 4b around the $[01\bar{1}0]$ matrix zone axis under the diffraction vector of $\boldsymbol{g} = [0002]$. According to the "$\boldsymbol{g}\cdot\boldsymbol{b} = 0''$ invisibility criterion, all ⟨a⟩ dislocations are invisible under the diffraction vector

Please cite this article as: F. Han, X. Luo, Q. Liu et al., The effect of grain size and rolling reduction on microstructure evolution and annealing hardening response of a Mg-3Gd alloy, Journal of Magnesium and Alloys, https://doi.org/10.1016/j.jma.2023.09.025

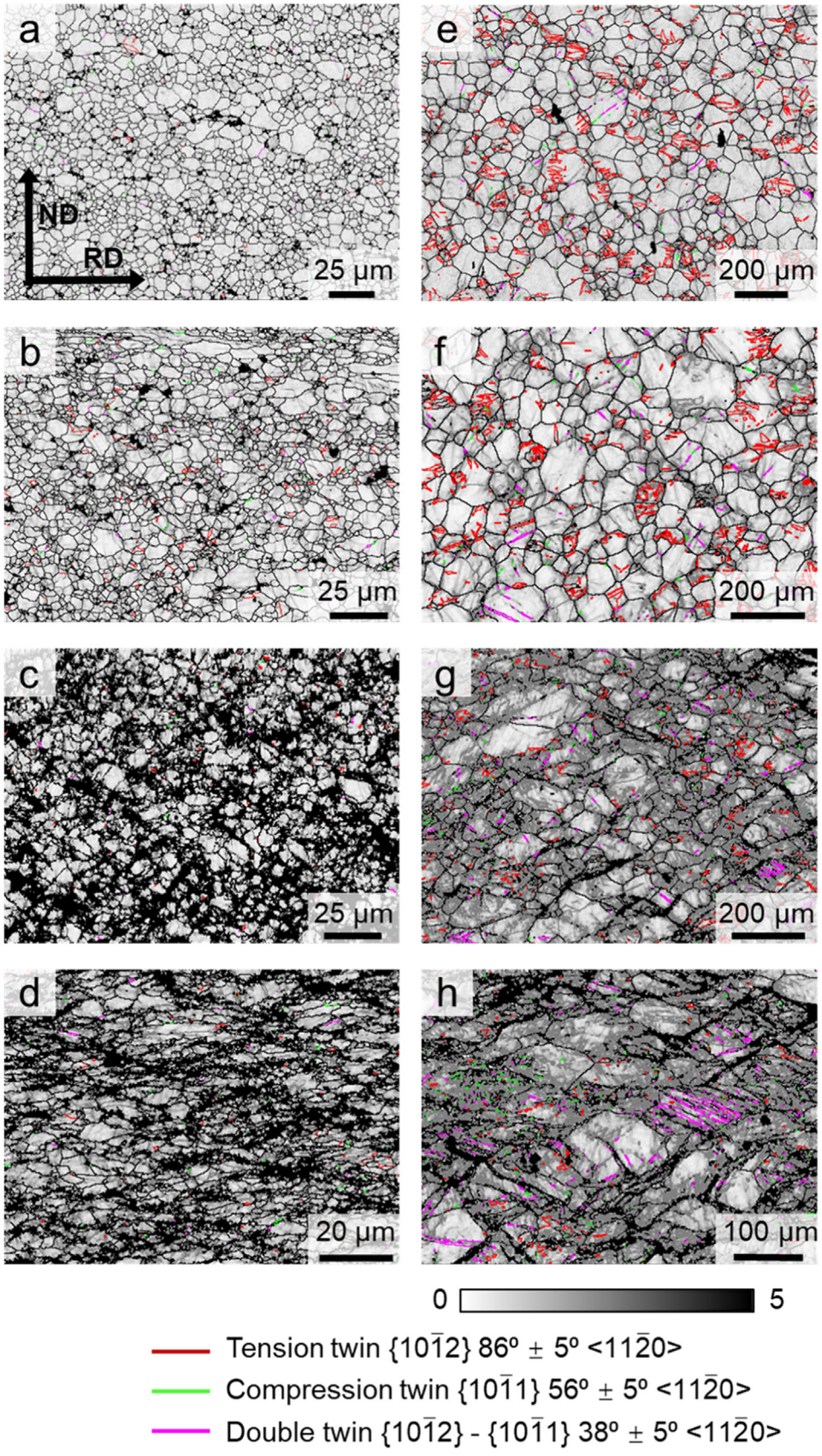

Fig. 3. KAM (Kernel Average Misorientation) maps coupled with various TBs of rolled FG and CG samples after being subjected to different rolling reductions: (a) FGcr5%, (b) FGcr10%, (c) FGcr20%, (d) FGcr40%, (e) CGcr5%, (f) CGcr10%, (g) CGcr20% and (h) CGcr40%. TTWs, CTWs and DTWs are colored in red, green and fuchsia lines, respectively.

Please cite this article as: F. Han, X. Luo, Q. Liu et al., The effect of grain size and rolling reduction on microstructure evolution and annealing hardening response of a Mg-3Gd alloy, Journal of Magnesium and Alloys, https://doi.org/10.1016/j.jma.2023.09.025

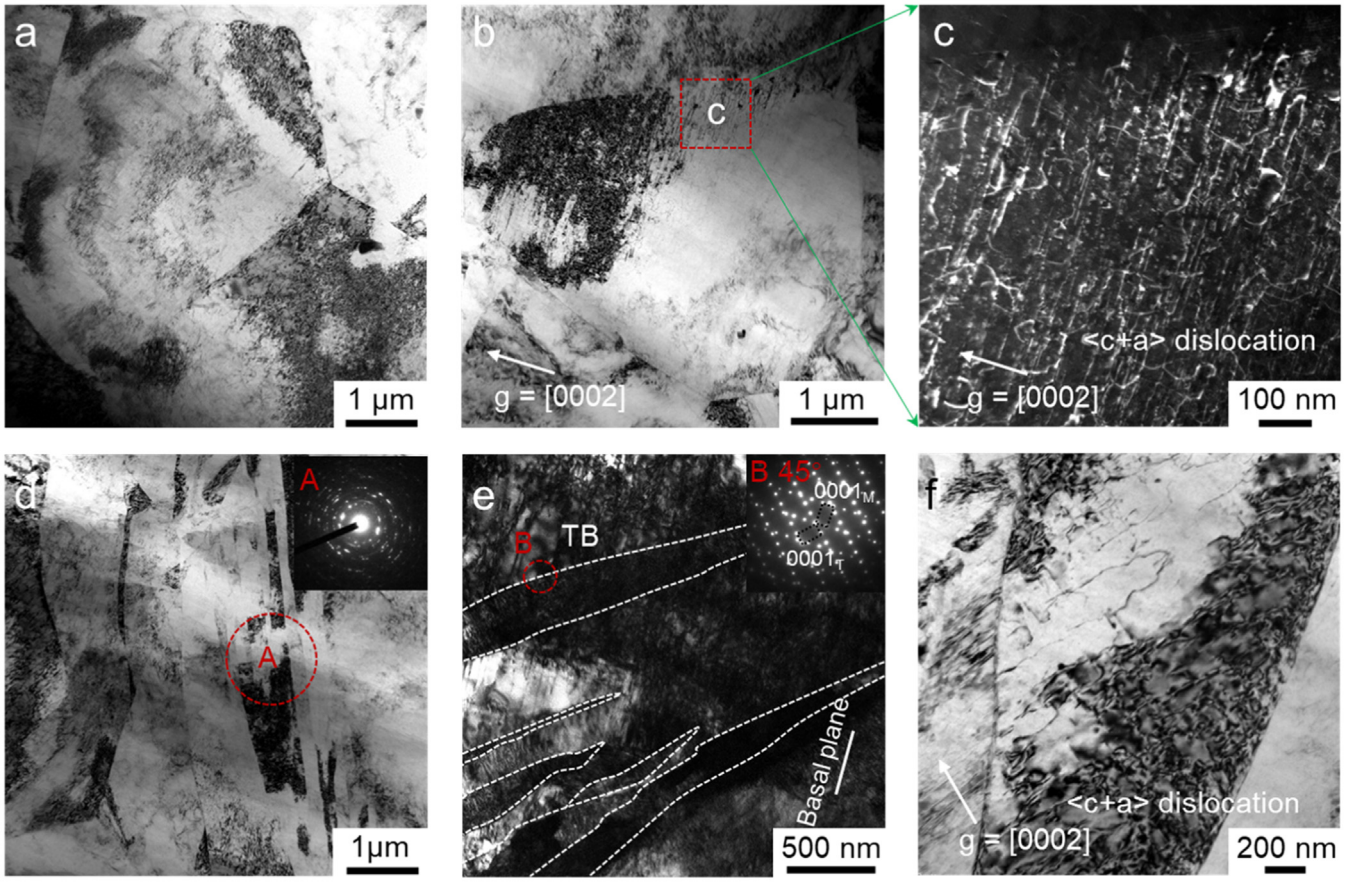

Fig. 4. TEM images of FGcr10% sample (a−c) and CGcr10% sample (d−f): (a) dislocation structures with high-density of dislocation tangles, (b) the weak-beam bright image under diffraction vector of $\boldsymbol{g} = [0002]$ and (c) the dark-field image magnified from the red dashed frame of (b). (d) Typical twin structures with lamellar TBs parallel to each other, (e) some separate twins with a high-density of dislocations inside the deformation matrix, and (f) the weak-beam bright-field image under diffraction vector of $\boldsymbol{g} = [0002]$. Selected area electron diffraction (SAED) patterns of the twin/matrix in the insets in (d) and (e) are obtained from the red dashed circles A and B, respectively.

Table 1
Quantitative structural parameters of FG and CG samples under various conditions based on the TEM microstructural characterization.

Samples	Microstructure				
	Dislocation structures	Twin structures		UFG structures	
	Vol. (%)	Twin thickness (nm)	Vol. (%)	Grain size (nm)	Vol. (%)
FGcr10%	95	212 ± 140	5	/	/
CGcr10%	77	523 ± 257	23	/	/
FGcr40%	65	122 ± 59	7	107 ± 43	28
FGcr40% +200 °C/1 h	61	125 ± 48	9	115 ± 38	30
CGcr40%	54	157 ± 73	36	116 ± 48	10
CGcr40% +200 °C/1 h	50	160 ± 65	37	124 ± 46	13

of $\boldsymbol{g} = [0002]$. Therefore, in Fig. 4c, the dislocations seen in the deformed matrix are pyramidal $\langle c + a \rangle$ dislocations, which exhibit high activity. Fig. 4d shows numerous twins in the CGcr10% sample, which consist of multiple lamellar twin structures arranged parallel to each other and enclosed by TBs. The selected area electron diffraction (SAED) pattern of the multiple twins is inserted (see inset A). In addition, as shown in Fig. 4e, separate twins are frequently observed in the deformation matrix of CGcr10% sample. The obtained SEAD pattern of inset B from the red dashed circle B shows that the misorientation angle of twin/matrix is 45°/[11$\bar{2}$0]. Moreover, the volume fraction of twin structures and average twin thickness in the CGcr10% sample are 23%, 523 ± 257 nm, respectively. Meanwhile, many dislocations parallel to the basal plane are clearly visible, which were determined to be basal ⟨a⟩ dislocations. The basal plane trace

Please cite this article as: F. Han, X. Luo, Q. Liu et al., The effect of grain size and rolling reduction on microstructure evolution and annealing hardening response of a Mg-3Gd alloy, Journal of Magnesium and Alloys, https://doi.org/10.1016/j.jma.2023.09.025

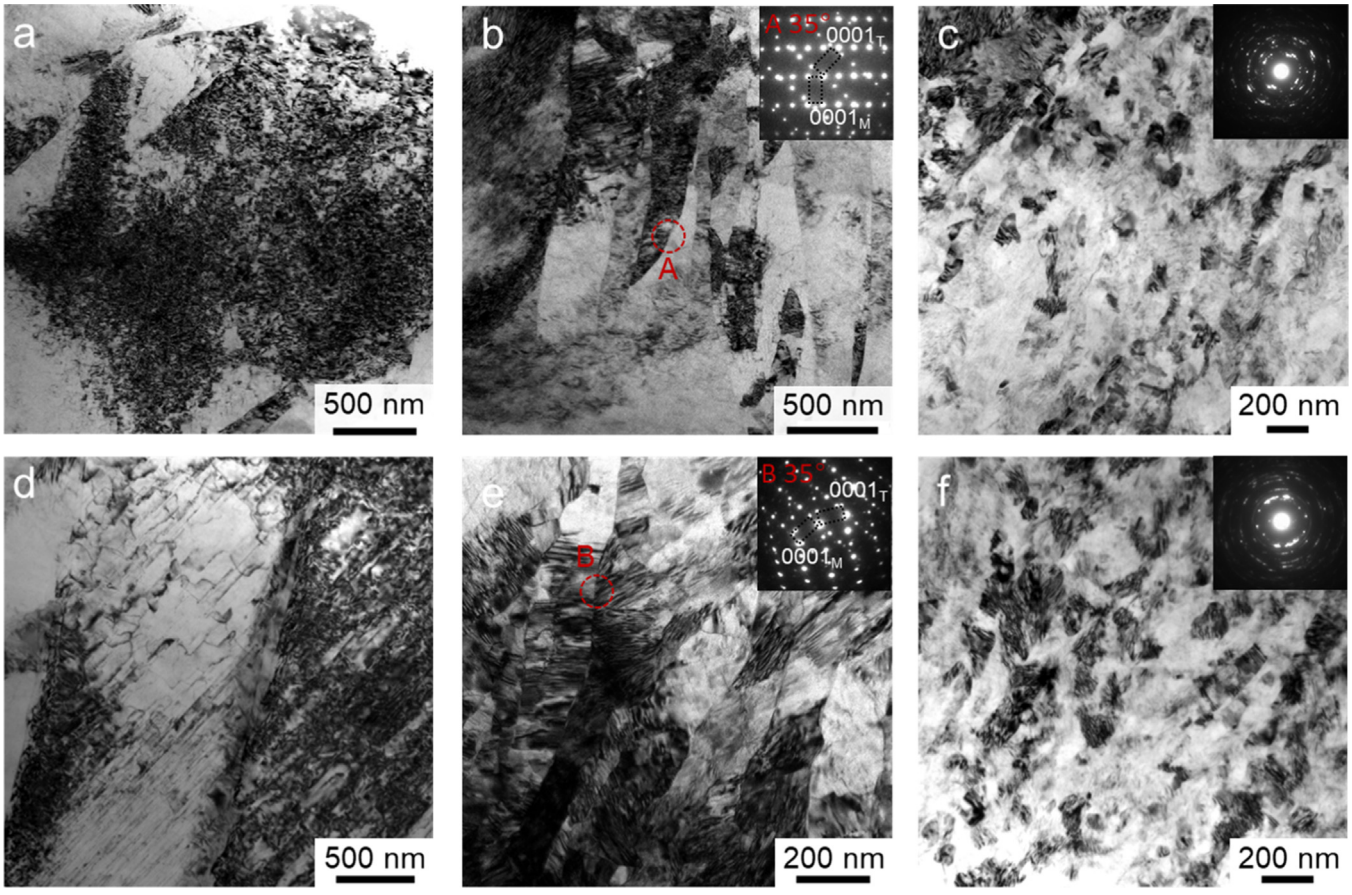

Fig. 5. TEM images of FGcr40% sample (a−c) and CGcr40% sample (d−f): (a, d) dislocation structures consisting of high-density dislocations, (b, e) typical twin structures with lamellar TBs approximately parallel to each other, (c, f) UFG structures. SAED patterns of twin/matrix and ultra-fined grains area are also provided in the upper right insets.

is marked by a solid white line. Fig. 4f shows a weak-beam bright-field image around the $[01\bar{1}0]$ matrix zone axis, which was taken with the diffraction vector of $\boldsymbol{g} = [0002]$. A few pyramidal $\langle c + a \rangle$ dislocations can also be seen in the deformation twin of CGcr10% sample. Therefore, after 10% rolling reduction, numerous basal and non-basal dislocations have been activated in the FGcr10% and CGcr10% samples. The main difference between the two rolled samples is that the CGcr10% sample contains much more deformation twins than the FGcr10% sample, which is consistent with the EBSD results. It is noted that the twins of CGcr10% sample are much coarser than those in the FGcr10% sample.

Fig. 5 shows representative TEM images of FGcr40% and CGcr40% samples. After 40% rolling reduction, dislocation structures with a higher dislocation density appear in the FGcr40% and CGcr40% samples, as shown in Figs. 5a and d. Meanwhile, plenty of severely plastically deformed areas have been refined to the sub-micrometer scale. As shown in Fig. 5b, some twin structures containing a few lamellar twins are occasionally observed. These lamellar twins align in the same direction, which is similar to those of the CGcr10% sample. The SAED pattern of inset A in Fig. 5b shows that the misorientation angle of twin/matrix in the red circle area is $35°/[11\bar{2}0]$, indicating that this TB belongs to DTWs. The twinning behavior is strongly inhibited in the FGcr40% sample due to initial fine grains, leading to a volume fraction and average twin thickness of only 7% and 122 ± 59 nm, respectively. Fig. 5c shows a typical TEM image of the UFG structures, which have a relatively lower dislocation density than that of the surrounding deformation matrix, resulting from multiple slip systems being activated as a structural refinement mechanism. Plenty of UFGs, together with dislocation entanglements, are observed as well. The large orientation spread is illustrated through the SAED pattern in the inset of Fig. 5c, indicating the presence of many of HAGBs. The average grain size and volume fraction of UFG structures are 107 ± 43 nm, 28%, respectively.

However, the deformation microstructure of the CGcr40% sample is obviously different from that of the FGcr40% sample. In addition to the dislocation structures shown in Fig. 5d, numerous adjacent lamellar twin structures with lamellar boundaries approximately parallel to each other are observed due to the activation of multiple twinning systems after 40% rolling reduction, as shown in Fig. 5b. The average twin thickness is 157 ± 73 nm, and the volume fraction of twin structures is 36%, see Table 1. The precise TEM characterization of twin structures is obtained from the $[11\bar{2}0]$ zone axis of the twin/matrix. The twin structures contain a few

Please cite this article as: F. Han, X. Luo, Q. Liu et al., The effect of grain size and rolling reduction on microstructure evolution and annealing hardening response of a Mg-3Gd alloy, Journal of Magnesium and Alloys, https://doi.org/10.1016/j.jma.2023.09.025

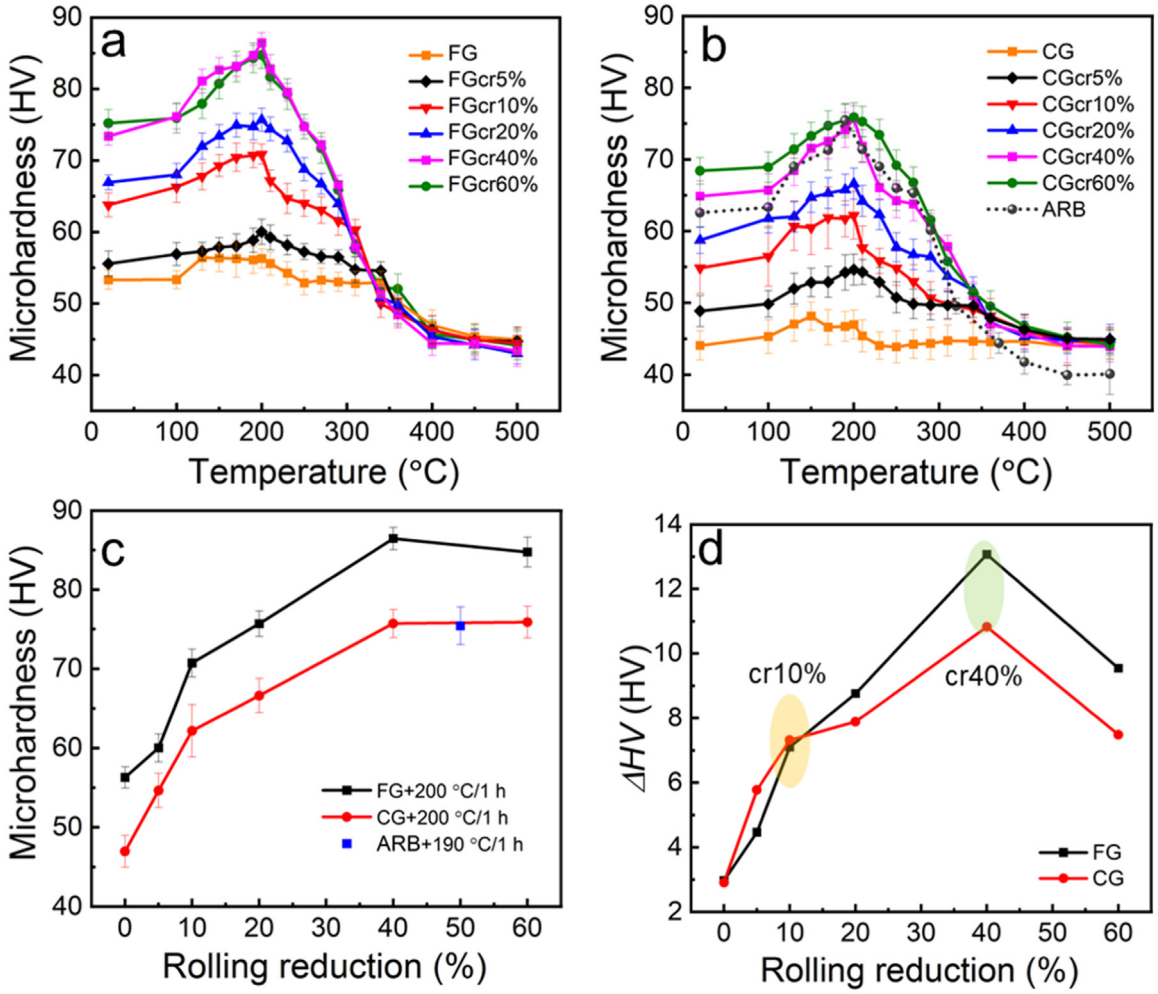

Fig. 6. Isochronal annealing curves of FG sample (a) and CG sample (b) after being subjected to different rolling reductions, where the microhardness of ARB-processed Mg-3Gd alloy during annealing showed as a dotted gray line in (b). (c) The peak microhardness of FG and CG samples at different rolling reductions (annealed at 200 °C for 1 h) and ARB sample (annealed at 190 °C for 1 h), (d) ΔHV of FG and CG samples before and after annealing at 200 °C for 1 h as a function of rolling reduction.

deformation twins, high-density SFs inside twins and plenty of dislocations. These SFs are parallel to the basal planes of deformation twins. Therefore, the CGcr40% sample forms a high-volume fraction of twin structures, much more than that of the FGcr40% sample. Moreover, the twins are much finer, and the TBs become more curved than those in the FGcr10% and CGcr10% samples. Meanwhile, some UFG structures exist, as shown in Fig. 5f, similar to that of the FGcr40% sample. The average grain size, 116 ± 48 nm, is slightly larger than that in the FGcr40% sample, while the volume fraction (10%) is much smaller.

3.2. Annealing hardening response

3.2.1. Isochronal annealing

Figs. 6a and b show the isochronal annealing curves of FG and CG samples deformed to different rolling reductions. The microhardness of annealed Mg-3Gd alloy samples prepared by accumulative roll-bonding (ARB) reported by Luo et al. [14] is also plotted as a dotted gray line in Fig. 6b. Clearly, both non-deformed FG and CG samples show a limited annealing hardening response within the annealing temperature range. For all rolled FG and CG samples, an enhanced annealing hardening response is observed as compared with their annealed non-deformed samples. When the annealing temperatures are below 250 °C, the microhardness of annealed samples is higher than that of the as-rolled samples, indicating the annealing hardening response is stronger than the recovery softening response. Additionally, it is worth noting that the peak microhardness values of all rolled samples are obtained at a temperature of about 200 °C. In addition, the peak microhardness of the annealed samples is almost constant when the rolling reduction is increased from 40% to 60%, which can be associated with similar deformation microstructures and limited Gd content in the present alloy. Recently, Luo et al. [23] reported that the initial sample of an Mg-3Gd alloy with an average grain size of 45 μm showed no annealing hardening response, whereas ARB-processed (hot rolling, $\varepsilon = 0.5$) samples experienced an enhanced annealing hardening response and obtained a peak microhardness of 75 ± 2

HV after annealing at 190 °C for 1 h. In the present work, the CGcr40% sample (the solid fuchsia curve in Fig. 6b with an initial grain size of 54 μm shows a similar hardening response to that of the ARB-processed sample (the dotted gray curve in Fig. 6b) during annealing. Moreover, Fig. 6c shows the peak microhardness curves of rolled FG and CG samples after annealing at 200 °C for 1 h and the peak microhardness value of ARB-processed sample annealed at 190 °C for 1 h. Clearly, with increasing rolling reduction, the peak microhardness curve of annealed FG samples remains above that of annealed CG samples. Interestingly, the peak microhardness for both annealed FG and CG samples shows the most rapid increase at 10% rolling reduction as compared with their initial samples. With further increasing rolling reduction, the peak microhardness of both annealed FG and CG samples gradually increases with a similar trend and reaches a saturation value at 40% rolling reduction. The achieved highest peak microhardness values are 86 ± 1 HV and 76 ± 2 HV, respectively, for annealed FG and CG samples. Note that the peak microhardness of the annealed ARB-processed sample is 75 ± 1 HV, which clearly is close to that of the CGcr40% sample. Fig. 6d shows ΔHV of FG and CG samples before and after annealing at 200 °C for 1 h as a function of rolling reduction, showing a clear difference in annealing hardening behavior between the deformed FG and CG samples. For the non-deformed FG and CG samples, the ΔHV value is limited, only 3 HV after annealing at 200 °C for 1 h. After 5% rolling reduction, the ΔHV value of the CGcr5% sample is slightly higher than that of the FGcr5% sample. When increasing the rolling reduction to 10% (marked by a yellow ellipse), the peak microhardness increments of annealed FGcr10% and CGcr10% samples both exceed 7 HV. Further increasing the rolling reduction to 40% (marked by a green ellipse), the ΔHV values of FGcr40% and CGcr40% samples increase to 13 HV and 11 HV, respectively. Moreover, when the rolling reduction is 60%, the ΔHV values of both FGcr60% and CGcr60% samples start to decrease. Clearly, the annealing hardening response of rolled FG and CG samples strongly depends on the rolling reduction, whereas the pattern of grain size effect on the annealing hardening response is more complicated (to be discussed later in this paper).

3.2.2. Isothermal annealing

To further understand the effect of grain size and rolling reduction on the annealing hardening response of Mg-3Gd alloy, isothermal annealing at three temperatures 150, 200 and 250 °C was carried out for the two initial non-deformed FG and CG samples and for 10% and 40% cold rolled FG and CG samples, i.e., FGcr10%, FGcr40%, CGcr10% and CGcr40%. Fig. 7 shows the annealing hardening curves for the FGcr10% (a), FGcr40% (b), CGcr10% (c) and CGcr40% (d) samples (in solid lines) annealed at 150, 200 and 250 °C. The annealing hardening curves of the initial non-deformed FG samples and CG samples (in dashed lines) annealed at 150 °C and 200 °C are included in Fig. 7, respectively, for comparison. As shown in Fig. 7, minor microhardness increments are observed in the initial FG and CG samples after isothermal annealing at 150 °C and 200 °C. However, for cold rolled FG and CG samples, the evolution of microhardness during isothermal annealing shows a strong annealing temperature dependence. When annealing at 150 °C, the microhardness of FGcr10% sample increases gradually from the initial 64 ± 2 HV to 75 ± 2 HV after annealing for 100 h, generating an increment of 11 HV (see Fig. 7a). The microhardness of FGcr40% sample increases rapidly from 73 ± 1 HV to 82 ± 2 HV during the first 20 min, and then steadily increases to 91 ± 2 HV at 100 h, resulting in a total increment of 18 HV (see Fig. 7b). It should be noted that FGcr10% and FGcr40% samples have not reached the peak-microhardness condition after annealing at 150 °C for 100 h, and that the ΔHV value of the FGcr40% sample is much more than that of the FGcr10% sample. When the annealing temperature is increased to 200 °C, FGcr10% and FGcr40% samples reach their peak microhardness values of 71 ± 1 HV and 86 ± 1 HV, respectively, within 1 h. Afterwards, the microhardness values of FGcr10% and FGcr40% samples decrease slightly to 69 ± 2 HV after 2 h and 84 ± 1 HV after 5 h, respectively, and then a plateau of the microhardness is obtained up to 100 h. With further increasing the annealing temperature to 250 °C, only a limited annealing hardening response is observed in the FGcr10% and FGcr40% samples. Their peak microhardness, 67 ± 2 HV and 78 ± 2 HV, respectively, are reached at 20 min, followed by a slow decrease during further annealing. It can be seen that the trend of the annealing hardening curves in the CGcr10% and CGcr40% samples is quite similar to that in the FGcr10% and FGcr40% samples at different annealing temperatures (see Figs. 7c and d). The maximum microhardness is 67 ± 3 HV and 77 ± 2 HV for the CGcr10% and CGcr40% samples, respectively, after annealing at 150 °C for 100 h, which both exceeds 12 HV of the microhardness of corresponding rolled conditions. The CGcr10% and CGcr40% samples annealed at 200 °C obtain a peak microhardness of 62 ± 3 HV and 76 ± 2 HV after 1 h of annealing, respectively. Afterwards, both keep stable values until 100 h experiencing only a slight decrease. Furthermore, during annealing at 250 °C, the CGcr10% sample shows a limited annealing hardening response within 20 min, and softening in the subsequent annealing until 100 h. The CGcr40% sample shows a slight decrease, instead of any hardening response, during annealing at 250 °C. Based on the aforementioned results, the maximum microhardness and ΔHV at different annealing temperatures are given in Table 2. The most evident difference in the microhardness increment is seen between the FGcr40% and CGcr40% samples during isothermal annealing at 150 °C.

3.3. XRD analysis

Fig. 8a shows the XRD patterns of FGcr40% and CGcr40% samples in the cold rolled state and after annealing at 200 °C for 1 h. All the diffraction peaks correspond to

Please cite this article as: F. Han, X. Luo, Q. Liu et al., The effect of grain size and rolling reduction on microstructure evolution and annealing hardening response of a Mg-3Gd alloy, Journal of Magnesium and Alloys, https://doi.org/10.1016/j.jma.2023.09.025

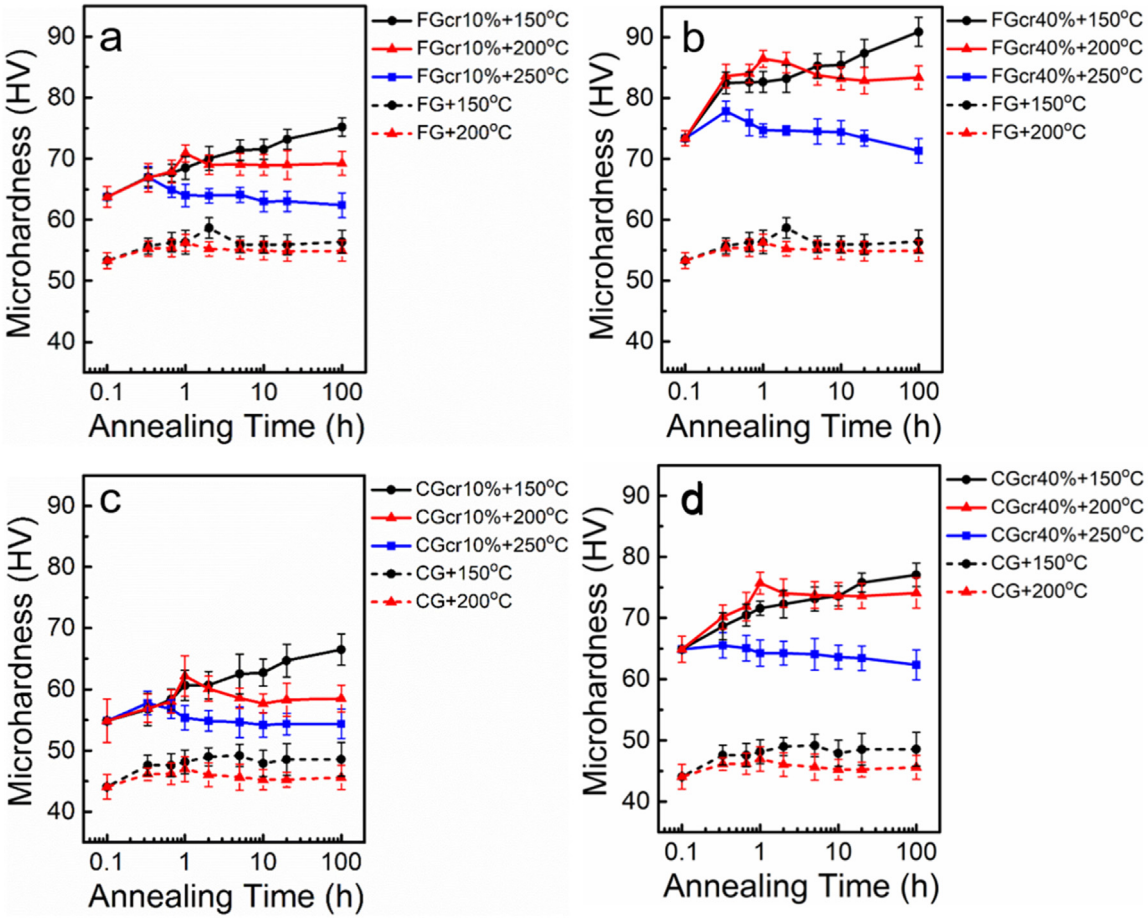

Fig. 7. Isothermal annealing curves of (a) FGcr10%, (b) FGcr40%, (c) CGcr10% and (d) CGcr40% samples. Annealing hardening curves of the initial FG and CG samples (in dashed lines) annealed at 150 °C and 200 °C are also included. The first data point corresponds to the microhardness of the initial non-deformed or cold rolled sample state.

Table 2
The maximum microhardness and ΔHV at different annealing temperatures (unit: HV).

Samples	As-rolled	150 °C	200 °C	250 °C	$\Delta HV_{150\ °C}$	$\Delta HV_{200\ °C}$	$\Delta HV_{250\ °C}$
FGcr10%	64 ± 2	75 ± 2	71 ± 2	67 ± 2	11	7	3
CGcr10%	55 ± 3	67 ± 3	62 ± 3	58 ± 2	12	7	3
FGcr40%	73 ± 2	91 ± 2	86 ± 2	78 ± 2	18	13	5
CGcr40%	65 ± 2	77 ± 2	76 ± 2	66 ± 2	12	11	1

the α-Mg phase. The {002} crystal planes show the highest peak intensity due to the strong basal textures of the samples. Moreover, the peak intensities of typical crystal planes of {002}, {101}, {102}, {112} and {104} exhibit only small changes after annealing, indicating little change in texture [46,48]. Fig. 8b shows that the dislocation densities of FGcr40% and CGcr40% samples decrease after annealing at 200 °C for 1 h. In addition, the lattice axial ratios (c/a) of both annealed samples increase compared to the corresponding rolled samples. This observation indicates that the crystal lattice distortion introduced by deformation is reduced by annealing.

3.4. Segregation of solute atoms along boundaries

3.4.1. Solute segregation in deformed samples

Generally, the chemical composition of all solute atomic columns can be traced and distinguished based on the HAADF-STEM images. In this work, for the deformed samples, the FGcr10% sample is used as an example to observe solute segregation along boundaries. As shown in Figs. 9a and b, a brighter contrast along a boundary inside the grain is observed, implying that segregation of heavier atoms occurs at such boundaries after plastic deformation. The corresponding fast Fourier transform (FFT) pattern in Fig. 9(c) shows

Please cite this article as: F. Han, X. Luo, Q. Liu et al., The effect of grain size and rolling reduction on microstructure evolution and annealing hardening response of a Mg-3Gd alloy, Journal of Magnesium and Alloys, https://doi.org/10.1016/j.jma.2023.09.025

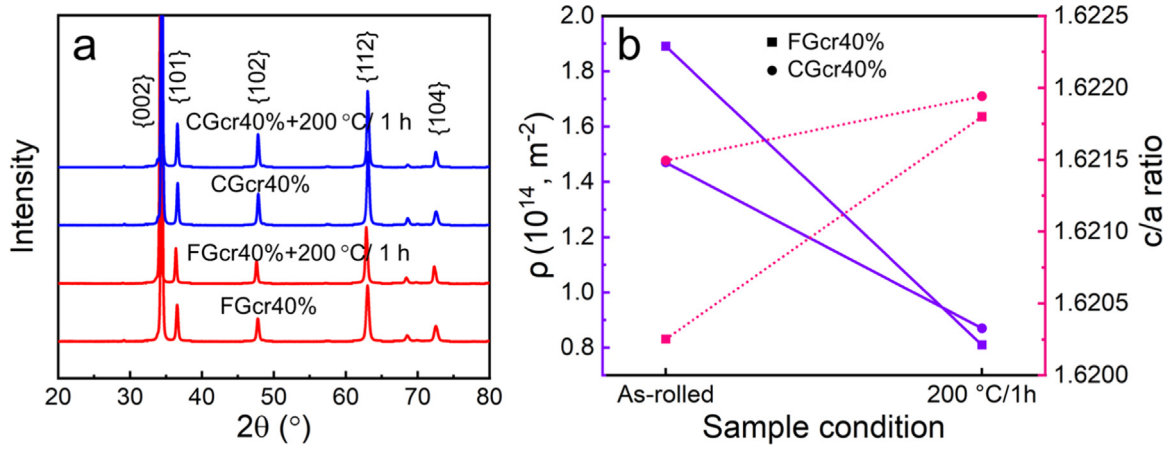

Fig. 8. (a) Overview of XRD patterns of FGcr40% and CGcr40% samples before and after annealing at 200 °C for 1 h, (b) the dislocation density and lattice axial ratio (c/a) of rolled and annealed samples.

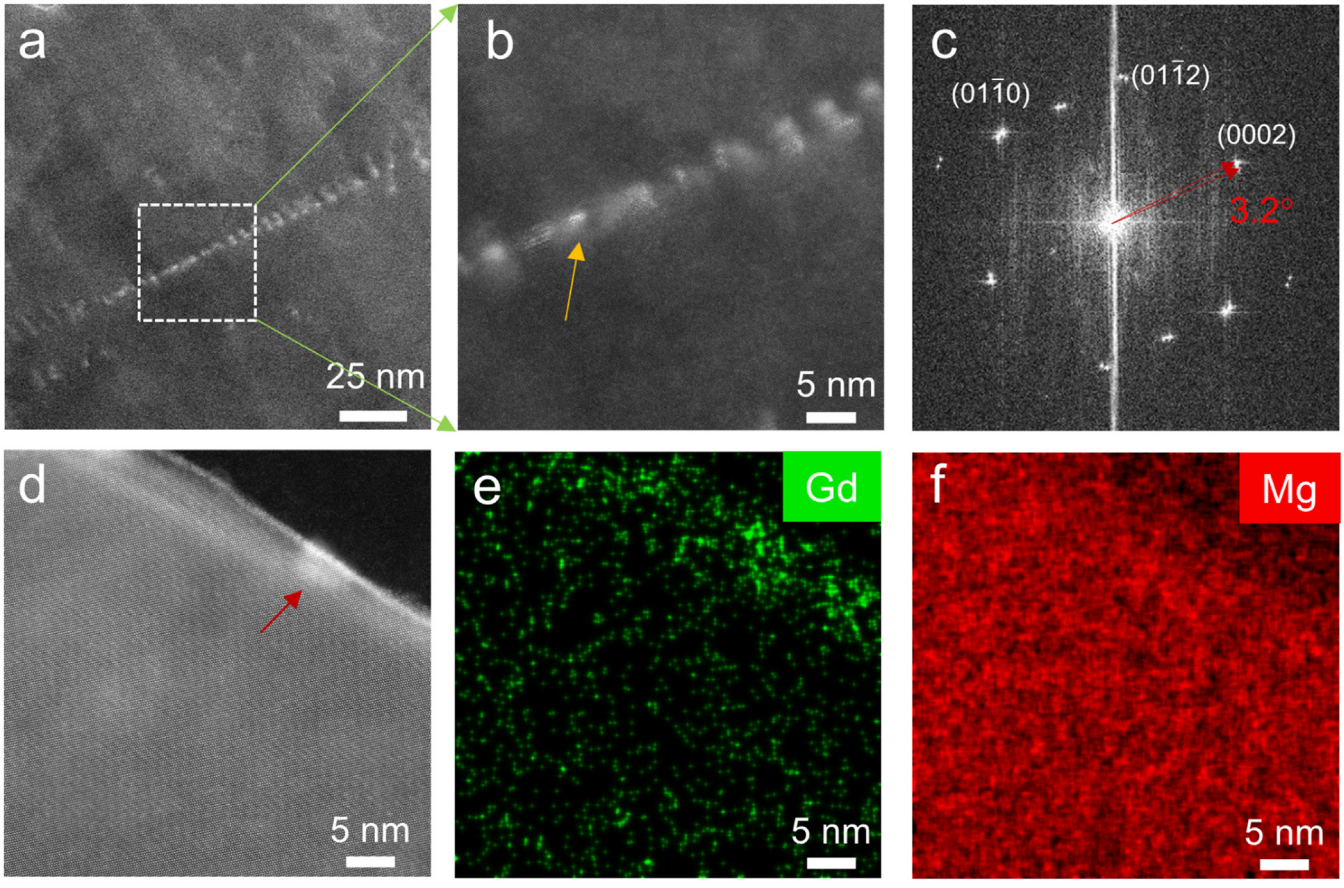

Fig. 9. HAADF-STEM images of FGcr10% sample: (a) the solute segregation along a LAGB, (b) the high magnification of white frame in (a), (c) the fast Fourier transform (FFT) pattern of (b), (d) the solute segregation along a GB; (e, f) corresponding Gd and Mg EDS mappings, respectively.

that this boundary is a LAGB of 3.2°. Fig. 9c shows the atomic-scale HAADF-STEM image of a region that includes a GB. Weak solute segregation along the GB is observed. The brighter contrast area in Fig. 9d (marked by a red arrow) could be a cluster. Figs. 9e and f show corresponding Gd and Mg energy dispersive spectrometer (EDS) mappings, respectively. The mappings in red and green are used to mark the distribution of Mg and Gd elements, respectively. Apparently, they provide clear evidence that the Gd atoms have segregated along this GB. Consequently, the brighter atomic columns along boundaries could be Gd-rich columns in the deformed Mg-3Gd alloy.

In order to further highlight the solute segregation of deformed samples, Fig. 10 shows an APT reconstruction that

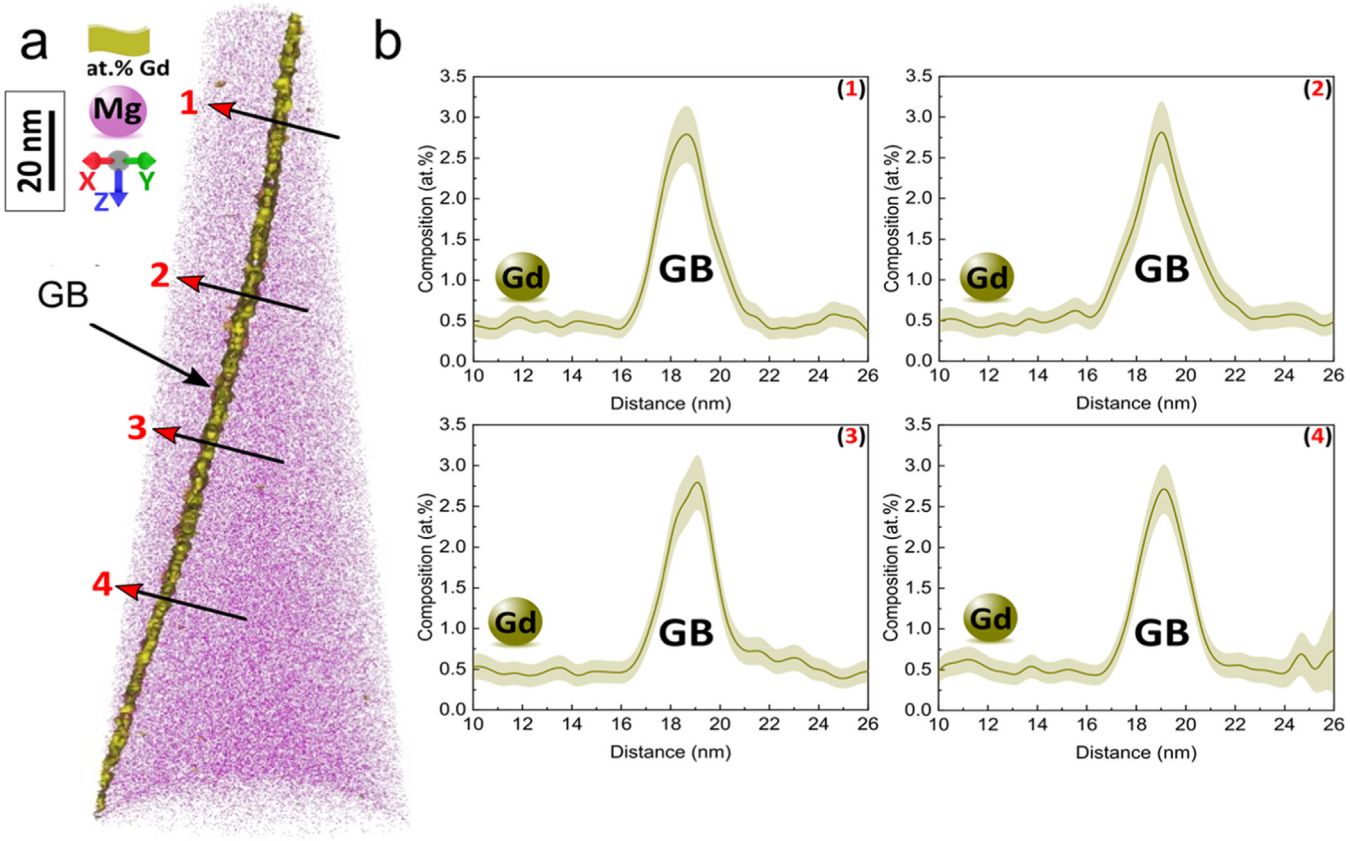

Fig. 10. (a) 3D elemental distribution of Gd atoms along a GB in FGcr10% sample using 2 at.% Gd isoconcentration, (b) Gd 1D concentration-depth concentration profiles across the GB quantified from 4 ROIs (marked by 4 black arrows) in (a).

contains a GB from the FGcr10% sample. In particular, Fig. 10a shows the three-dimensional elemental distribution of Gd atoms along a GB, presented in terms of 2 at.% Gd isoconcentration surface. Clearly, besides Gd segregation at this GB, there is no remarkable elemental partitioning in the grain interior. For further determining the concentration gradient across the GB and adjacent matrix, the local concentration fluctuations across the GB are quantified by cylindrical regions of interest (ROI) perpendicular to the GB plane. Fig. 10b shows Gd 1D concentration-depth concentration profiles across the GB obtained from 4 ROIs (marked by 4 black arrows) in (a). A strong segregation behavior of Gd atoms at the GB occurs, with the local Gd concentration in the boundary region reaching a maximum value of 2.92 at.%. By contrast, the Gd concentration in the grain interior is 0.48 at.%.

3.4.2. Solute segregation in annealed samples

The HAADF-STEM/EDS and APT results of FGcr10% sample provide strong evidence of rolling-induced Gd segregation along the boundaries of deformed samples. To evaluate the effect of annealing treatment on Gd segregation of rolled samples, CGcr40% and CGcr40%+200 °C/1 h samples are selected as typical examples for characterization. Figs. 11a and d show the TEM images of CGcr40% and CGcr40%+200 °C/1 h samples, respectively. Similar lamellar twin structures with high-density SFs are observed in both samples, indicating that the microstructures are quite stable and no apparent grain coarsening occurs. The twin thickness remains almost the same with a marginal increase from 157 nm to 160 nm, and the average grain size of UFG structures increases from 107 nm to 115 nm, as given in Table 1. Figs. 11b and c show a weak bright contrast at some boundaries along $[1\bar{2}10]$ zone axis, indicating the weak solute segregation in the CGcr40% sample. By contrast, after annealing at 200 °C for 1 h, a much brighter contrast at GBs, LAGBs and TBs is observed than in the deformation matrix, suggesting a remarkable Gd segregation at these boundaries, as shown in Figs. 11e and f. In addition, a significant periodic distribution of Gd clusters (marked by red arrows) inside grains and twins is frequently observed.

Fig. 12 shows the HAADF-STEM images at atomic resolution in CGcr40%+200 °C/1 h sample. Figs. 12a and b show an obvious Gd segregation along LAGBs and GBs. It can be seen that there is a remarkable difference in solute segregation between LAGBs and GBs. The matrix in Fig. 12a consists of sub-grains misoriented by 6.7° by these LAGBs and the corresponding FFT pattern is shown in the upper right inset. Clearly, the distributed Gd atoms along LAGBs are discontinuous and periodic, indicating the LAGBs are occupied alternately by Mg and Gd atoms. However, a continuous and dense Gd distribution along GBs is observed in Fig. 12b, which is further substantiated in Figs. 12c and d by corre-

Please cite this article as: F. Han, X. Luo, Q. Liu et al., The effect of grain size and rolling reduction on microstructure evolution and annealing hardening response of a Mg-3Gd alloy, Journal of Magnesium and Alloys, https://doi.org/10.1016/j.jma.2023.09.025

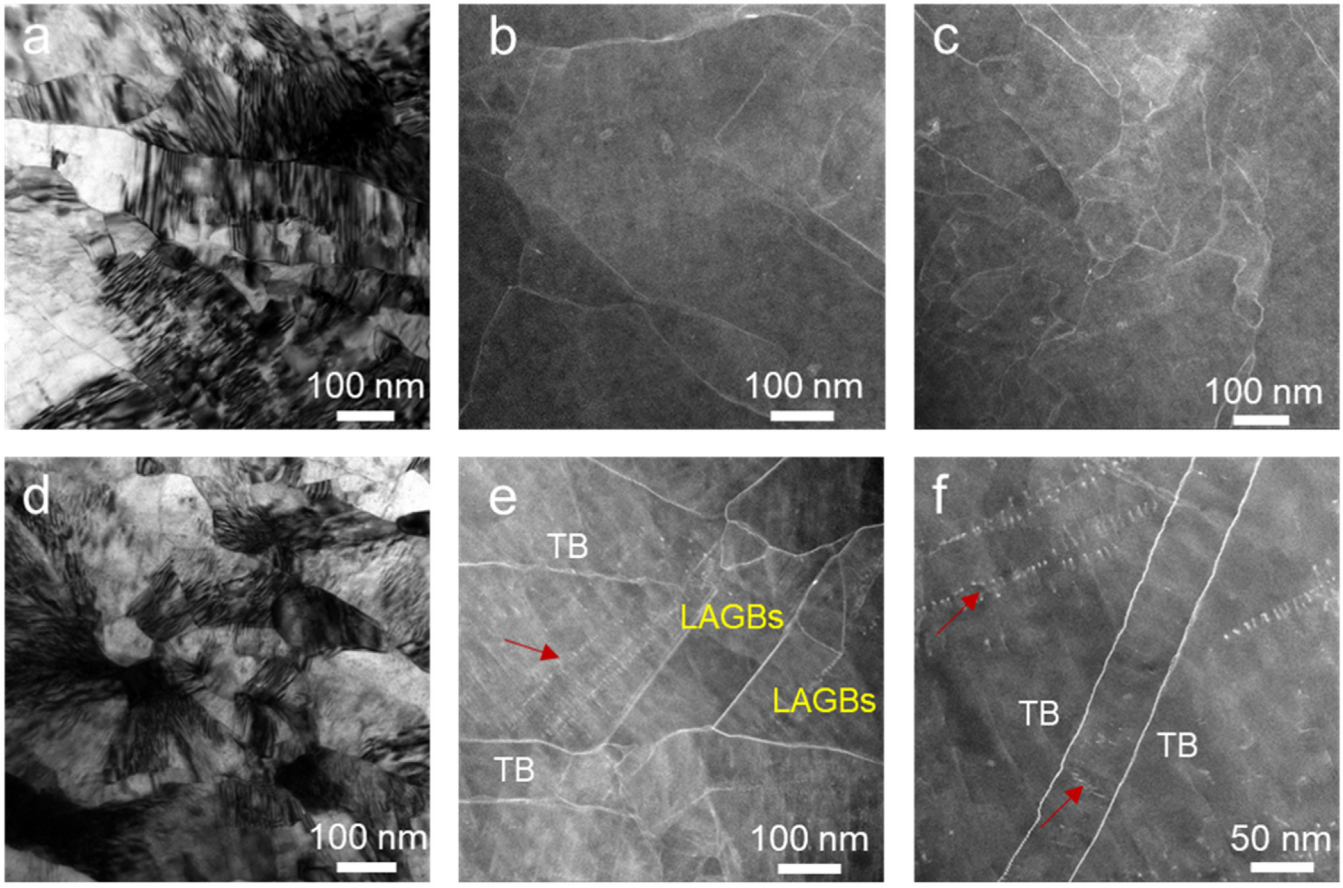

Fig. 11. The bright field TEM and HAADF-STEM images of CGcr40% (a−c) and CGcr40%+200 °C/1 h (d−f) samples: (a, d) typical twin structures, (b, c) the weak solute segregation along boundaries, (e, f) the strong solute segregation along TBs, LAGBs and dislocation boundaries.

sponding Gd in green and Mg in red EDS mappings obtained from the yellow frame of Fig. 12b, respectively. A periodic Gd distribution along TBs similar to the Gd segregation along LAGBs is observed in Fig. 12e. According to the FFT pattern in Fig. 12e, the misorientation relationship between the twin and matrix is determined to be a typical 56.5° $<11\bar{2}0>$ CTW. Moreover, an insignificant Gd segregation can also be seen along SFs inside twins. Fig. 12f shows clear Gd clusters periodically segregated along a LAGB with 7.5° misorientation (see the FFT pattern of the inset). According to the inverse FFT image in Fig. 12g obtained from the {0001} reflection, it can be observed that the Gd clusters are strongly segregated at dislocation cores. Meanwhile, the geometric phase analysis (GPA) method, which is sensitive to minor displacements of lattice fringes, is used to evaluate the micro-strain distribution around the dislocation cores of Fig. 12f, as shown in Fig. 12h. The blue and red represent compression and tension regions of dislocation cores, respectively. Generally, the solute atoms with a larger radius than that of Mg atoms (1.595 Å) tend to migrate to the tension regions in Mg alloys [16]. Therefore, the Gd atoms tend to occupy tension regions (red regions) of dislocation cores due to the larger radius of Gd atoms (1.822 Å) than Mg atoms. As such, the segregation of Gd atoms is beneficial to improve the stability of boundaries and impede dislocation annihilation.

4. Discussion

The deformed and annealed microstructures and annealing hardening response of Mg-3Gd alloy with respect to both FG and CG samples under various rolling reductions have been investigated in the present study. It is demonstrated that the annealing hardening response is strongly enhanced by deformation, which strongly depends on initial grain size, rolling reduction and annealing temperature.

4.1. Effect of grain size and rolling reduction on deformation microstructure

The dominant deformation mechanisms of Mg alloys and resultant deformation microstructures rely on many factors, such as rolling reduction, alloying elements and grain size [19,24,49]. As shown in Figs. 3−5, the recrystallized grains in the FG and CG samples evolve differently during cold rolling, which is ascribed to the significant difference in dislocation and twinning activities caused by the initial different grain sizes prior to deformation. In the rolled FG samples, twinning behavior is strongly inhibited from 5% to 40% rolling reductions due to the higher CRSS [47]. With increasing rolling reduction, the dislocation density gradually increases, resulting in the rearrangement of dislocations and microstructural

Please cite this article as: F. Han, X. Luo, Q. Liu et al., The effect of grain size and rolling reduction on microstructure evolution and annealing hardening response of a Mg-3Gd alloy, Journal of Magnesium and Alloys, https://doi.org/10.1016/j.jma.2023.09.025

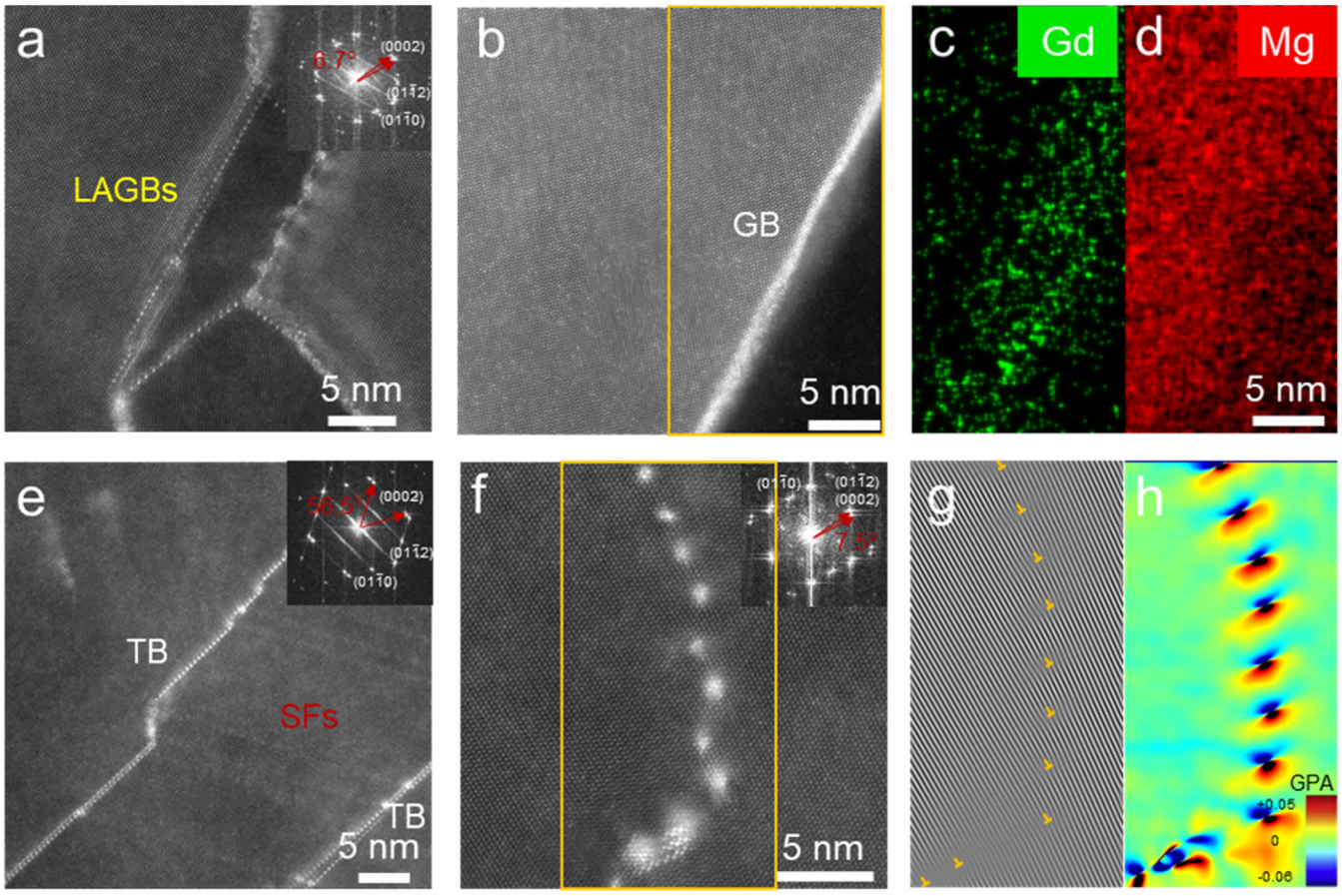

Fig. 12. The HAADF-STEM images at atomic resolution in CGcr40%+200 °C/1 h sample: (a, b) the distinct and periodic solute segregation along LAGBs and GBs, respectively. (c, d) Corresponding Gd and Mg EDS mappings in the yellow frame of (b), respectively; (e, f) solute segregation along TBs, SFs and dislocation cores, respectively. The corresponding FFT patterns of (a, e, f) are also provided as the upper right insets. (g) The inverse FFT image in the yellow frame of (f) obtained from {0001} reflection, in which dislocation cores are marked with yellow symbols "⊥", (h) corresponding GPA distortion map of {0001} plane.

refinement. However, in addition to the dislocation accumulation in the rolled CG samples, with increasing rolling reduction, the multiple twinning modes are activated and interact with high-density dislocations, resulting in a microstructural refinement. Thus, this phenomenon also indicates that the deformation twinning is strongly dependent on the initial grain size, whereas the activation of dislocation slip only shows a weak grain size dependence [50,51]. After 10% rolling reduction, both FGcr10% and CG10% samples exhibit high activities of dislocation slip. The most remarkable difference between FGcr10% and CGcr10% samples is the type and number of deformation twins. Numerous deformation twins with a volume fraction of 23% lead to significant grain refinement in the CGcr10% sample. Especially, after 40% rolling reduction, microstructural refinement is observed in FGcr40% and CGcr40% samples due to the severe plastic deformation, indicating the activation and interaction of multiple slip modes and twinning systems.

All structural parameters of rolled samples with 10% and 40% rolling reduction are given in Table 3. Based on these data sets, the relationship among D_E, S_{total} and rolling reduction is shown in Fig. 13. It is worth noting that, for

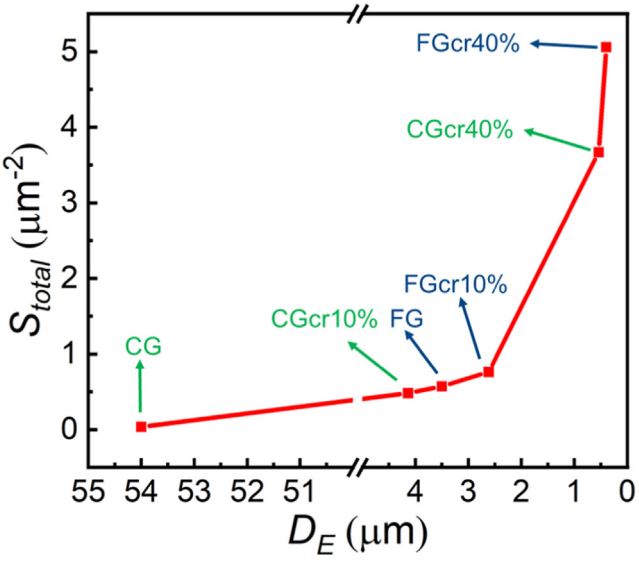

Fig. 13. The relationship between the equivalent grain size (D_E) and the total surface area per volume (S_{total}) in the initial and rolled FG and CG samples.

Table 3
Quantitative structural parameters of initial and rolled FG and CG samples based on EBSD data and TEM microstructures.

Samples	D_R (μm)[a]	$Vol.^{GB}$ (%)	D_{UFG} (μm)[b]	$Vol.^{UFG}$ (%)	D_{twin} (μm)[c]	$Vol.^{twin}$ (%)	S_{total} (μm^{-2})[d]	D_E (μm)[e]
FG	3.5	100	–	–	–	–	0.57	3.5
CG	54.0	100	–	–	–	–	0.04	54.0
FGcr10%	3.8	100	–	–	0.212	5	0.76	2.6
CGcr10%	47.0	100	–	–	0.523	23	0.48	4.2
FGcr40%	3.5	65	0.107	28	0.122	7	5.06	0.4
CGcr40%	54.0	54	0.116	10	0.157	36	3.67	0.5

[a] Average grain size.
[b] Average grain size of UFG structures.
[c] Twin thickness of twin structures.
[d] Total surface area per volume of boundaries.
[e] Equivalent grain size.

the FGcr10% and CGcr10% samples, the D_R is the average grain size without considering TBs obtained from EBSD results. GBs are hardly destroyed after 10 rolling reduction; thus, the $Vol.^{GB}$ is regarded as 100%. In addition, for the FGcr40% and CGcr40% samples, the D_R is the average grain size of initial FG and CG samples. It can be observed that the S_{total} increases with increasing rolling reduction in both FG and CG samples. After 10% rolling reduction, the difference in S_{total} between FGcr10% and CGcr10% samples is insignificant. However, after 40% rolling reduction, the S_{total} of FGcr40% sample is much larger than CGcr40% samples. Therefore, a strong grain size effect on S_{total} probably influences the solute segregation in the Mg-3Gd alloy and, as a consequence the annealing hardening response.

4.2. Annealing hardening response controlled by Gd segregation

4.2.1. Effect of deformation on the annealing hardening response

According to previous studies [14,32,48,52], it has been found that the Gd content of the Mg-3Gd alloy, in general, is too low to form substantial strengthening precipitates. Consistent with these findings, the initial FG and CG samples show only a slight annealing hardening response during both isochronal and isothermal annealing. However, after cold rolling, the annealing hardening response of rolled samples is effectively enhanced with increasing rolling reduction. All rolled samples obtain an increased peak microhardness with increasing rolling reductions after annealing at 200 °C for 1 h. In the present study, a strong segregation tendency of Gd atoms at various boundaries is observed by the HAADF-STEM/EDS results of annealed samples, which can effectively enhance the annealing hardening response in the deformed Mg-3Gd alloy, similar to that observed in ref. [14,16,53], where dense Gd atoms are segregated periodically at tension regions along different TBs, SFs, GBs and dislocation cores. In addition, it can be seen from Fig. 6 that the contribution from the annealing hardening response to the microhardness of rolled samples is closely related to the rolling reduction. At a small rolling reduction (5%), there is a low density of boundaries, and the Gd segregation provides insignificant hardening after annealing. With an increase to 40% rolling reduction, the density of boundaries increases, providing increased sites and decreased diffusion distance for segregation. Consequently, stronger Gd segregation leads to enhanced hardening after annealing. However, if the rolling reduction is too large, then the deformed samples may have excessive amounts of boundaries but insufficient solute atoms to segregate at boundaries, causing a dilution of segregation. Additionally, the boundaries are unstable, and dislocations can readily annihilate during annealing, leading to a limited hardening response. Thus, the peak microhardness of annealed samples increased with increasing rolling reduction, and it reached a saturation value at 40% rolling reduction. This phenomenon is consistent with the relationship between the annealing hardening response and strain observed in Mg-Zn-Ca alloy [35]. Meanwhile, the isothermal annealing microhardness results of rolled 10% and 40% samples during 150−250 °C in Fig. 7 further evidence that the rolling reduction has an essential role in the contribution of the hardening response to the microhardness of annealed samples. The plausible reason for this is the origin of the difference in deformation microstructure and its evolution during annealing. After 10% rolling reduction, the deformation microstructure only involves the activation and interaction of dislocation slips and twinning systems. However, 40% rolling reduction leads to the formation of additional substructures, such as UFG structures and lamellar twin structures. The different dominant deformation microstructures are likely to affect Gd segregation at various boundaries and further influence the contribution of annealing hardening on the microhardness.

4.2.2. Grain size effect on the annealing hardening response

Undeniably, the annealing hardening response of FG and CG samples is simultaneously enhanced with increasing rolling reductions, and the peak microhardness of the rolled FG samples remains higher than that of the rolled CG samples after annealing. In addition, the microstructures of the rolled FG and CG samples are significantly different due to their different initial grain sizes, whereas the annealing hardening response exhibits an insignificant grain size effect at the small strains (< 20%) during annealing. With increasing the rolling reduction to 40%, the grain size effect on the annealing hard-

Please cite this article as: F. Han, X. Luo, Q. Liu et al., The effect of grain size and rolling reduction on microstructure evolution and annealing hardening response of a Mg-3Gd alloy, Journal of Magnesium and Alloys, https://doi.org/10.1016/j.jma.2023.09.025

ening response becomes relatively obvious, which is closely related to deformation microstructures. After being subjected to the lower strains (< 20%), the deformation microstructure of the FG sample is dislocation-dominated, whereas that of the CG sample is dominated by a high density of twins coexisting with dislocations. Moreover, the deformation twins in the rolled CG samples lead to a remarkable grain refinement compared with that of rolled FG samples, indicating the formation of more TBs. However, there is no apparent difference in S_{total} between FGcr10% and CGcr10%, leading to a similar annealing hardening response. With further increasing the rolling reduction to 40%, in addition to high-density dislocations, these are UFG structures and lamellar twin structures formed in the local severely deformed regions of rolled FG and CG samples. Finally, the S_{total} used for solute segregation of the FGcr40% is larger than that of the CGcr40% sample, leading to a stronger annealing hardening response in the FGcr40% sample, which is further substantiated by the isothermal annealing results in Fig. 7. On the one hand, the maximum ΔHV values of rolled samples decreases with the temperature increasing from 150 °C to 250 °C, which means that the annealing temperature has an essential influence on the microhardness evolution of samples. Generally, the mobility of thermally activated boundaries (M) can be expressed as follows [54]:

$$M=M_0\exp\left(\frac{-Q}{k_BT}\right) \tag{8}$$

where M_0, T, k_B and Q is a pre-exponential constant, absolute temperature, Boltzmann constant and activation energy, respectively. Therefore, it is not beneficial to maintain the grain boundary stability to increase annealing temperature. Meanwhile, the accelerated dislocation annihilation further leads to the softening response. In addition, the higher temperature can improve the migration of solute atoms and further enhance solute segregation along different TBs, SFs, GBs and dislocation cores. Therefore, under the competitive effect of softening and segregation hardening response, the rolled samples annealed at 150 °C for 100 h acquire the maximum microhardness. On the other hand, the maximum ΔHV values of FGcr10% and CGcr10% samples are almost the same at the different annealing temperatures from 150 °C to 250 °C (see Table 2). However, for the FGcr40% and CGcr40% samples, there is a remarkable difference in maximum ΔHV value, especially at 150 °C, which means the initial grain size has a significant effect on the annealing hardening response. In addition, all ΔHV values are higher than 0, which means the segregation hardening response is stronger than the softening response. In short, the grain size effect on the annealing hardening response is strongly affected by rolling reduction and annealing temperature based on the microhardness results during annealing, which can be related to the type and density of boundary defects caused by deformation.

4.2.3. Annealing hardening mechanisms

After cold rolling and subsequent annealing, the microhardness of Mg-3Gd alloy is strongly increased. Considering annealing treatment and the ΔHV in more detail, FGcr40% and CGcr40% after annealing 200 °C for 1 h are used as examples to analyze the hardening mechanisms. The contribution of GBs, dislocations, solid solution and solute segregation to the microhardness of the samples will be discussed.

The contribution of GB hardening (ΔHV_{GB}) can be assessed by the Hall-Petch relationship [45]:

$$\Delta HV_{GB} = Ck_{HP}d^{-1/2} \tag{9}$$

where k_{HP} is the Hall-Petch slope for Mg alloys, d is the grain size (here, we use the equivalent grain size, D_E). The TEM microstructures of FGcr40% and CGcr40% after annealing 200 °C for 1 h are very stable due to the Gd segregation along boundaries. The grain size of UFG structures and the twin thickness of twin structures only slightly increase, leading to a marginal increase of D_E. Therefore, after annealing, the contribution of GB strengthening is only slightly reduced.

The contribution of dislocation hardening (ΔHV_D) is closely related to dislocation density, which is generally accepted to be expressed as [44,55]:

$$\Delta HV_D = CM\alpha_1 Gb\sqrt{\rho} \tag{10}$$

where M is the Taylor factor, α_1 is a constant, G is the shear modulus, b is the length of the Burgers vector, ρ is the dislocation density. Based on the XRD analysis, it can be seen that after annealing 200 °C for 1 h, the corresponding dislocation densities of FGcr40% and CGcr40% samples are decreased from 1.89×10^{14} m^{-2} to 0.81×10^{14} m^{-2}, 1.48×10^{14} m^{-2} to 0.87×10^{14} m^{-2}, respectively, leading to the decrease of dislocation hardening.

For the contribution of solid solution hardening (ΔHV_{ss}), it can be estimated by the relationship [46]:

$$\Delta HV_{SS} = Ck_{Gd}\times\varkappa_{Gd}^{2/3} \tag{11}$$

where k_{Gd} is a constant related to the Gd element, and $\varkappa_{Gd}$ is the equilibrium concentration of Gd atoms for the Mg matrix. After annealing 200 °C for 1 h, the lattice axial ratios (c/a) of FGcr40% and CGcr40% samples are slightly increased from 1.6203 to 1.6218, and from 1.6215 to 1.6219 (Fig. 8b), respectively, which means that the amount of Gd atoms dissolved in the α-Mg matrix is reduced. Moreover, this is further demonstrated by the more obvious Gd segregation at boundaries in the annealed samples than that of rolled samples (see Figs. 11 and 12). Therefore, $\varkappa_{Gd}$ is decreased, leading to a decreased solid solution hardening contribution.

According to the change mentioned above in hardening contribution after annealing 200 °C for 1 h, it can be concluded that an annealing treatment will inevitably cause a softening response and decrease the microhardness of the samples. However, after annealing, the microhardness of FGcr40% and CGcr40% samples still shows an increase of more than 10 HV, which indicates a remarkable annealing hardening effect of Gd segregation. The microhardness increment in annealed FG samples is mainly contributed by Gd segregation along dislocation boundaries, while in the annealed CG samples, Gd segregation along dislocation and twin boundaries provides most hardening response. Therefore, solute segregation-induced and solute clustering-assisted

Please cite this article as: F. Han, X. Luo, Q. Liu et al., The effect of grain size and rolling reduction on microstructure evolution and annealing hardening response of a Mg-3Gd alloy, Journal of Magnesium and Alloys, https://doi.org/10.1016/j.jma.2023.09.025

hardening can be used as one of the important approaches to strengthen Mg alloys. Based on the good combination of rolling reduction and annealing treatment, controlling the diffusion and precipitation of solute atoms can optimize the microstructure and properties of Mg alloys, which provides a new perspective for the design of high-performance Mg alloys.

5. Conclusions

In this work, we have demonstrated that grain size and rolling reduction play a crucial role in the dominant deformation microstructures, which could further significantly affect the annealing hardening response of an Mg-3Gd alloy. From the combined thorough microstructural characterization and microhardness analysis, the main conclusions can be drawn as follows:

1. Deformation twinning is highly suppressed, and multiple dislocation activities increase with increasing rolling reduction in the fine-grained (with an average grain size of 3.5 μm) sample. After undergoing 40% rolling reduction, the deformation microstructure is refined and forms ultra-fine grain structures with a volume fraction of ∼28%. However, the early deformation of the coarse-grained (with an average grain size of 54 μm) sample is dominated by twinning. After 10% rolling reduction, numerous twins with a volume fraction of ∼23% form. When the rolling reduction increases to 40%, multiple twinning systems are activated and form twin structures with a volume fraction of ∼36%, co-existing with high-density dislocations.
2. The annealing hardening response of Mg-3Gd alloy can be effectively accelerated and enhanced by deformation compared to non-deformed samples. With increasing rolling reduction, the peak microhardness of rolled samples increases after annealing and reaches to a saturation value at 40% rolling reduction. The microhardness of annealed samples is the competitive result of the softening response and segregation hardening response, which is influenced by rolling reduction, grain size and annealing temperature and time. Furthermore, the grain size effect on annealing hardening response is insignificant at lower rolling reductions (< 20%), whereas the grain size effect becomes evident as rolling reduction increases to 40%, which is probably associated with the difference in the density of boundaries.
3. Room temperature deformation (cold rolling) induces Gd segregation along boundaries (such as grain boundaries, twin boundaries, stacking faults and dislocations) of fine-grained and coarse-grained samples, which improves the stability of grain boundaries. Subsequent annealing treatment can further promote the boundary segregation of Gd atoms and provide an outstanding hardening response, which completely resists the inevitable softening response caused by grain coarsening and dislocation annihilation.

Declaration of Competing Interest

The authors declare no potential conflict of interest.

Acknowledgements

The authors gratefully acknowledge the financial support from the National Key Research and Development Program of China (No. 2021YFB3702101), National Natural Science Foundation of China (No. 52130107, 52071038), Fundamental Research Funds for the Central Universities (No. 2023CDJXY-018), the “111” Project (No. B16007) by the Ministry of Education and the State Administration of Foreign Experts Affairs of China. The Research Council of Norway (RCN) is acknowledged for its support to the Norwegian Micro- and Nano-Fabrication Facility, NorFab (No. 295864), the Norwegian Laboratory for Mineral and Materials Characterization, MiMaC (No. 269842/F50), the RCN INRPART project IntMat (No. 309724) and the Center for Research based Innovation SFI PhysMet (No. 309584).

References

[1] S.R. Agnew, J.F. Nie, Scr. Mater. 63 (2010) 671–673.
[2] W.J. Joost, P.E. Krajewski, Scr. Mater. 128 (2017) 107–112.
[3] Y. Yang, X. Xiong, J. Chen, X. Peng, D. Chen, F. Pan, J. Magnes. Alloys 9 (2021) 705–747.
[4] M.H. Yoo, J.K. Lee, Philos. Mag. A 63 (1991) 987–1000.
[5] S.R. Agnew, O. Duygulu, Int. J. Plast. 21 (2005) 1161–1193.
[6] B.C. Suh, M.S. Shim, K.S. Shin, N.J. Kim, Scr. Mater. 84-85 (2014) 1–6.
[7] R. Zheng, T. Bhattacharjee, A. Shibata, T. Sasaki, K. Hono, M. Joshi, N. Tsuji, Scr. Mater. 131 (2017) 1–5.
[8] R. Zheng, T. Bhattacharjee, S. Gao, W. Gong, A. Shibata, T. Sasaki, K. Hono, N. Tsuji, Sci. Rep. 9 (2019) 11702.
[9] J.F. Nie, X. Gao, S.M. Zhu, Scr. Mater. 53 (2005) 1049–1053.
[10] C.M. Cepeda-Jiménez, M. Castillo-Rodríguez, M.T. Pérez-Prado, Acta Mater 165 (2019) 164–176.
[11] X. Gao, S.M. He, X.Q. Zeng, L.M. Peng, W.J. Ding, J.F. Nie, Mater. Sci. Eng. A 431 (2006) 322–327.
[12] J.F. Nie, Metall. Trans. A 43 (2012) 3891–3939.
[13] G. Wu, C. Wang, M. Sun, W. Ding, J. Magnes. Alloys 9 (2021) 1–20.
[14] X. Luo, Z. Feng, R. Fu, T. Huang, G. Wu, X. Huang, J. Alloys Compd. 819 (2020) 153051.
[15] M.Z. Bian, T.T. Sasaki, T. Nakata, Y. Yoshida, N. Kawabe, S. Kamado, K. Hono, Acta Mater 158 (2018) 278–288.
[16] J.F. Nie, Y.M. Zhu, J.Z. Liu, X.Y. Fang, Science 340 (2013) 957–960.
[17] N. Stanford, M.R. Barnett, Int. J. Plast. 47 (2013) 165–181.
[18] B.Q. Shi, Y.Q. Cheng, X.L. Shang, H. Yan, R.S. Chen, W. Ke, Mater. Sci. Eng. A 743 (2019) 558–566.
[19] L.L.C. Catorceno, H.F.G. De Abreu, A.F. Padilha, J. Magnes. Alloys 6 (2018) 121–133.
[20] J. Luo, W.W. Hu, Q.Q. Jin, H. Yan, R.S. Chen, Scr. Mater. 127 (2017) 146–150.
[21] J. Ye, X.P. Lin, T.B. Zhao, N.N. Liu, H.B. Xie, Y. Niu, F. Teng, Mater. Sci. Eng. A 663 (2016) 49–55.
[22] C.M. Cepeda-Jiménez, J.M. Molina-Aldareguia, M.T. Pérez-Prado, Acta Mater 88 (2015) 232–244.
[23] R. Lu, Z. Xu, F. Jiang, S. Xu, D. Fu, H. Zhang, J. Teng, J. Magnes. Alloys 11 (2021) 1461–1471.
[24] X. Luo, Z. Feng, T. Yu, J. Luo, T. Huang, G. Wu, N. Hansen, X. Huang, Acta Mater 183 (2020) 398–407.
[25] S.W. Lee, S.H. Kim, W.K. Jo, W.H. Hong, W. Kim, B.G. Moon, S.H. Park, J. Alloys Compd. 791 (2019) 700–710.

Please cite this article as: F. Han, X. Luo, Q. Liu et al., The effect of grain size and rolling reduction on microstructure evolution and annealing hardening response of a Mg-3Gd alloy, Journal of Magnesium and Alloys, https://doi.org/10.1016/j.jma.2023.09.025

[26] K. Wei, R. Hu, D. Yin, L. Xiao, S. Pang, Y. Cao, H. Zhou, Y. Zhao, Y. Zhu, Acta Mater 206 (2021) 116604.
[27] M.R. Barnett, Mater. Sci. Eng. A 464 (2007) 8–16.
[28] M.R. Barnett, Mater. Sci. Eng. A 464 (2007) 1–7.
[29] W.B. Hutchinson, M.R. Barnett, Scr. Mater. 63 (2010) 737–740.
[30] X.Y. Shi, Y. Liu, D.J. Li, B. Chen, X.Q. Zeng, J. Lu, W.J. Ding, Mater. Sci. Eng. A 630 (2015) 146–154.
[31] X. Luo, Z. Feng, T. Yu, T. Huang, R. Li, G. Wu, N. Hansen, X. Huang, Mater. Sci. Eng. A 772 (2020) 138763.
[32] X. Gao, J.F. Nie, Scr. Mater. 58 (2008) 619–622.
[33] X. Wang, Y. Hu, K. Yu, S. Mahajan, I.J. Beyerlein, E.J. Lavernia, T.J. Rupert, J.M. Schoenung, Scr. Mater. 209 (2022) 114375.
[34] Q. Wang, S. Chen, B. Jiang, Z. Jin, L. Zhao, J. He, D. Zhang, G. Huang, F. Pan, J. Magnes. Alloys 10 (2021) 3576–3588.
[35] Z.R. Zeng, Y.M. Zhu, M.Z. Bian, S.W. Xu, C.H.J. Davies, N. Birbilis, J.F. Nie, Scr. Mater. 107 (2015) 127–130.
[36] J. Chen, Z. Wang, X. Ma, X. Wang, Y. Lei, W. Yan, J. Alloys Compd. 642 (2015) 92–97.
[37] H. Fu, B. Ge, Y. Xin, R. Wu, C. Fernandez, J. Huang, Q. Peng, Nano Lett 17 (2017) 6117–6124.
[38] W.W. Jian, G.M. Cheng, W.Z. Xu, H. Yuan, M.H. Tsai, Q.D. Wang, C.C. Koch, Y.T. Zhu, S.N. Mathaudhu, Mater. Res. Lett. 1 (2013) 61–66.
[39] J.F. Nie, N.C. Wilson, Y.M. Zhu, Z. Xu, Acta Mater 106 (2016) 260–271.
[40] T. Huang, L. Shuai, A. Wakeel, G. Wu, N. Hansen, X. Huang, Acta Mater 156 (2018) 369–378.
[41] Y. Suzuki, K. Ueno, K. Murasawa, Y. Kusuda, M. Takamura, T. Hakoyama, T. Hama, S. Suzuki, Materials Science and Engineering: A 794 (2020) 139585.
[42] K. Thompson, D. Lawrence, D.J. Larson, J.D. Olson, T.F. Kelly, B. Gorman, Ultramicroscopy 107 (2007) 131–139.
[43] L. Lutterotti, S. Gialanella, Acta Mater 46 (1998) 101–110.
[44] W.T. Sun, X.G. Qiao, M.Y. Zheng, C. Xu, S. Kamado, X.J. Zhao, H.W. Chen, N. Gao, M.J. Starink, Acta Mater 151 (2018) 260–270.
[45] Y. Chen, N. Gao, G. Sha, S.P. Ringer, M.J. Starink, Acta Mater 109 (2016) 202–212.
[46] C. Liu, X. Chen, D. Tolnai, Y. Hu, W. Zhang, Y. Zhang, F. Pan, J. Mater. Sci. Technol. 144 (2023) 70–80.
[47] R. Zheng, J.P. Du, S. Gao, H. Somekawa, S. Ogata, N. Tsuji, Acta Mater 198 (2020) 35–46.
[48] J.P. Hadorn, T.T. Sasaki, T. Nakata, T. Ohkubo, S. Kamado, K. Hono, Scr. Mater. 93 (2014) 28–31.
[49] S. Sandlöbes, S. Zaefferer, I. Schestakow, S. Yi, R. Gonzalez-Martinez, Acta Mater 59 (2011) 429–439.
[50] M.R. Barnett, Scr. Mater. 59 (2008) 696–698.
[51] M.R. Barnett, Z. Keshavarz, A.G. Beer, D. Atwell, Acta Mater 52 (2004) 5093–5103.
[52] M. Bugnet, A. Kula, M. Niewczas, G.A. Botton, Acta Mater 79 (2014) 66–73.
[53] I. Basu, K.G. Pradeep, C. Mießen, L.A. Barrales-Mora, T. Al-Samman, Acta Mater 116 (2016) 77–94.
[54] R. Mahjoub, M. Ferry, N. Stanford, Computational Materials Science 210 (2022) 111042.
[55] M.J. Starink, X. Cheng, S. Yang, Acta Mater 61 (2013) 183–192.

Please cite this article as: F. Han, X. Luo, Q. Liu et al., The effect of grain size and rolling reduction on microstructure evolution and annealing hardening response of a Mg-3Gd alloy, Journal of Magnesium and Alloys, https://doi.org/10.1016/j.jma.2023.09.025